LOW-MASS STAR FORMATION TRIGGERED BY SUPERNOVAE IN PRIMORDIAL CLOUDS

Masahiro N. Machida

Center for Frontier Science, Chiba University, Yayoicho 1-33, Inageku, Chiba 263-8522, Japan; machida@cfs.chiba-u.ac.jp

Kohji Tomisaka

National Astronomical Observatory, Mitaka, Tokyo 181-8588, Japan; tomisaka@th.nao.ac.jp

Fumitaka Nakamura

Faculty of Education and Human Sciences, Niigata University, Ikarashi 2-8050, Niigata 950-2181, Japan; fnakamur@ed.niigata-u.ac.jp

and

Masayuki Y. Fujimoto

Department of Physics, Hokkaido University, Sapporo 060-0810, Japan; fujimoto@astro1.sci.hokudai.ac.jp

ABSTRACT

The evolution of a gas shell, swept up by the supernova remnant of a massive first-generation star, is studied with H_2 and HD chemistry taken into account and with the use of a semianalytical approximation to the dynamics. When a first-generation star, formed in a parent pregalactic cloud, explodes as a supernova with explosion energy in the range of 10^{51}–10^{52} ergs at redshifts of $z = 10$–50, H_2 and HD molecules are formed in the swept up gas shell at fractional abundances of $\sim 10^{-3}$ and $\sim 10^{-5}$, respectively, and effectively cool the gas shell to temperatures of 32–154 K. If the supernova remnant can sweep to gather the ambient gas of mass 6×10^4 to 8×10^5 $M_\odot$, the gas shell comes to be dominated by its self-gravity and, hence, is expected to fragment. The amount of swept up gas necessary for fragmentation increases with the explosion energy and decreases with the interstellar gas density (or redshift) of the host cloud, which provides a lower boundary to the mass of the host cloud in which star formation is triggered by the first-generation supernova. Also, the condition for fragmentation is very sensitive to the thermal state of interstellar gas. Our result shows that for a reasonable range of temperatures (200–1000 K) of interstellar gas, the formation of second-generation stars can be triggered by a single supernova or hypernova with explosion energy in the above range in a primordial cloud of total (dark and baryonic) mass as low as a few times 10^6 $M_\odot$. For higher temperatures in the interstellar gas, however, the condition for the fragmentation in the swept up gas shell demands a larger supernova explosion energy. We also follow the subsequent contraction of the fragment pieces assuming their geometry (sphere and cylinder) and demonstrate that the Jeans masses in the fragments decrease to well below 1 $M_\odot$ by the time the fragments become optically thick to the H_2 and HD lines. The fragments are then expected to break up into dense cores whose masses are comparable to the Jeans masses and collapse to form low-mass stars that can survive to the present. If the material in the gas shell is mixed well with the ejecta of the supernova, the shell and low-mass stars thus formed are likely to have metals of abundance $[Fe/H] \simeq -3$ on average. This metallicity is consistent with those of the extremely metal-poor stars found in the Galactic halo. Stars with low metallicities of $[Fe/H] < -5$ such as HE 0107$-$5240, recently discovered in the Galactic halo, are difficult to form by this mechanism and must be produced in different situations.

Subject headings: cosmology: theory — early universe — galaxies: formation — molecular processes — stars: formation

Online material: color figures

1. INTRODUCTION

Star formation in the early universe is believed to have played a critical role in the formation and evolution of galaxies. Massive stars explode as supernovae (SNe) that may contribute to the cosmic reionization and metal pollution of the universe. Low-mass stars formed in the early universe must survive to the present and are expected to carry precious information from during or even previous to the early epoch of galaxy formation. Because of this importance, the process of star formation in the early universe has been attracting wide interest (e.g., Ostriker & Gnedin 1996; Uehara et al. 1996).

In the bottom-up scenarios of structure formation such as those of the cold dark matter models, the first collapsed objects should have formed at redshifts of $z \sim 10^2$–10 with mass scales of 10^5–10^8 $M_\odot$ (e.g., Haiman et al. 1996; Tegmark et al. 1997).

Stars ought to have been born in these first collapsed primordial clouds, totally lacking metals, before galaxies were formed. Such stars are referred to as first-generation stars. When the first collapsed objects are virialized, gas is first heated up to temperatures of $T \simeq 100 \ h^{2/3} \ (M/10^6 \ M_\odot)^{2/3}(1+z)$ K (Bromm et al. 2002) and hence needs to be cooled efficiently to collapse further into stars in these primordial clouds. Theoretical studies have suggested that in the first collapsed pregalactic objects, hydrogen molecules can form and cool the gas to temperatures of $T \simeq$ several $\times 10^2$ K, which leads to the formation of first-generation stars (e.g., Yoneyama 1972; Palla et al. 1983). First-generation stars are expected to be massive, or low-mass deficient, because of temperatures higher than those of the present interstellar matter (Bromm et al. 1999, 2002; Nakamura & Umemura 1999; Abel et al. 2000; but see Nakamura & Umemura 2001).

On the other hand, the number of extremely metal-poor stars found in our Galaxy has recently been increased substantially (more than 100 for stars with $[\mathrm{Fe/H}] < -3$) by large-scale surveys of the Galactic halo such as the HK survey (Beers et al. 1992 and see also Norris et al. 1999) and the Hamburg/ESO survey (Christlieb et al. 2001). In particular, one giant star, HE 0107$-$5240 with a metallicity of $[\mathrm{Fe/H}] = -5.3$, has been found very recently (Christlieb et al. 2002). For such low metallicities as $[\mathrm{Fe/H}] \lesssim -4$, metals contribute little to radiative cooling (Yoshii & Sabano 1980; Omukai 2000). The thermal property of such metal-poor gas has to be essentially the same as that of the primordial gas. The very existence of these low-mass stars with such extremely low metallicities is evidence of the operation of the mechanism to form low-mass stars efficiently in the gas clouds of primordial abundances, completely devoid of metals. From existent studies on the thermal evolution of primordial gas clouds, the asserted lack of low-mass stars among the first-generation stars is mainly ascribed to the scantiness of relic electrons ($[e/\mathrm{H}] \simeq 10^{-5}$ to 10^{-6}), which limits the formation of H_2 molecules necessary for the cooling of gas in the primordial clouds (e.g., Galli & Palla 1998; Bromm et al. 2002). The electron abundance can be larger, however, when gas in the primordial clouds is first heated above the temperatures of $\gtrsim 10^4$ K to be ionized and then undergoes cooling and recombination (Shapiro & Kang 1987). A larger fraction of free electrons will survive to yield the production of more abundant H_2 molecules primarily through the H^- process of $H + e^- \rightarrow H^- + h\nu$ and $H + H^- \rightarrow H_2 + e^-$. Accordingly, the gas clouds can be cooled effectively first by H_2 molecules and then by HD molecules to temperatures sufficiently low for the formation of low-mass stars.

There are two possible ways to achieve such situations in primordial clouds (e.g., Shapiro & Kang 1987; Ferrara 1998; Nishi & Susa 1999; Uehara & Inutsuka 2000). For primordial clouds more massive than $\sim 10^8 \, M_\odot$, the virialized temperatures at the collapse can be high enough to ionize the gas. For such massive clouds, however, we have to take into account the possible influence of pollution, prior to the collapse, of metals produced by the first-generation stars, since their collapse is delayed on average for more than $\sim 10^8$ yr as compared with the first collapsed clouds with masses of $\sim 10^6 \, M_\odot$ (Tegmark et al. 1997). The other way may be shock heating by supernova explosions of the first-generation stars. The ambient gas in the clouds must be swept up together, heated up, and ionized by the shock waves induced by the supernova explosions.

Tsujimoto et al. (1999) have proposed a scenario of consecutive star formation, triggered by supernovae, from an abundance analysis of the extremely metal-poor stars found in the Galactic halo. It is to be properly established, however, that a gas shell swept up by a supernova shock can actually fragment to form stars within the host clouds. Nishi & Susa (1999) discussed the condition of cloud disruption by supernovae with hydrogen chemistry taken into account. They argued that the scenario is possible only for massive first-collapsed objects with total masses larger than several times $10^7 \, M_\odot$. Since they did not solve the thermal evolution of supernova remnants (SNRs), however, the electron density and, hence, the resultant H_2 abundance may be underestimated, while the kinetic energy of SNRs is overestimated by applying the Sedov-Taylor solution to the later evolution. Ferrara (1998) discussed the notion that the gas, which is cooled to temperatures of ~ 300 K, is blown away from the cloud without fragmentation in his study of the thermal evolution of a shocked gas, taking into account the collective supernovae of the Population III objects of total masses from 10^6 to $10^7 \, M_\odot$.

Recently, Salvaterra et al. (2004) have studied star formation induced by primordial SNRs in first collapsed objects, taking into account the H_2 cooling. They suggested that a supernova shock can trigger formation of low-mass stars only when it is driven by an efficiently energetic supernova of explosion energy greater than 10^{52} ergs (e.g., hypernova or pair-instability supernova). In their calculations, they assumed that the interstellar matter in which the SNR expands is ionized by UV radiation of the progenitor star and its temperature remains constant at 10^4 K during the expansion of the SNR. The resulting high interstellar pressure tends to stall the expansion of the SNR shell, preventing the shell from sweeping and gathering enough gas to become self-gravitating. However, the temperatures of interstellar gas are likely to decrease to lower values because of efficient radiative cooling by H_2 molecules that are reformed in the interstellar gas on a timescale of less than 10^3–10^4 yr after the supernova explosion. This reduction in the ambient pressure may significantly affect the expansion of the SNR shell and changes the condition to trigger star formation. Bromm et al. (2003) have also performed smoothed particle hydrodynamics (SPH) simulations of such an SNR driven by a pair-instability supernova explosion due to a first-generation star. They showed that a high-energy supernova explosion (pair instability supernova) blows a minihalo of mass $10^6 \, M_\odot$ and gas with metallicity $Z \gtrsim 10^{-2} \, Z_\odot$ is ejected to the intergalactic space. However, they did not address the issue of star formation triggered by the first supernova itself.

In these previous works (Ferrara 1998; Salvaterra et al. 2004; Bromm et al. 2003), only H_2 molecules have been considered as the coolants after recombination. It should be pointed out, however, that under some conditions in the primordial clouds, deuterated hydrogen molecules, HD, become a more efficient coolant than H_2 (e.g., Puy et al. 1993; Galli & Palla 1998). For example, Uehara & Inutsuka (2000) have demonstrated that the HD cooling becomes dominant in the postshock gas with shock velocities larger than $\simeq 300$ km s^{-1}. Flower (2002) and Flower & Pineau des Forêts (2003) also investigated the effect of HD cooling on the fragmentation of primordial clouds. Nakamura & Umemura (2002a) found that if H_2 abundance exceeds a critical value of $\sim 3 \times 10^{-3}$, the thermal evolution of primordial clouds is controlled by HD cooling, which reduces the gas temperature to ~ 50–100 K (see also Nakamura & Umemura 2002b for more details). These studies indicate that HD cooling plays an important role in star formation in primordial gas clouds.

In this paper, we investigate the dynamical and thermal evolution of a gas shell swept up by an SNR in a first collapsed primordial cloud and discuss the possibility of the formation of low-mass stars that can survive to date. We take into account the chemistry of H_2 and HD molecules, and the evolution of an SNR is studied using a semianalytic formula, which enables us to sweep the large parameter space with a detailed treatment of the primordial chemistry. Uehara & Inutsuka (2000) have computed the evolution of a gas cloud for a particular initial condition and demonstrated that once the gas has been ionized, the HD molecule plays a dominant role in cooling and enables low-mass star formation. Our purpose is then to explore the conditions of the explosion energy and the redshift of supernovae in primordial clouds that can lead to low-mass star formation. First, we study whether the gas shell, swept up by an SNR, can break up into fragments as a result of cooling due to H_2 and HD molecules. Furthermore, we follow the evolution of the fragments into lower mass cores from which low-mass stars will be formed. In the computations, we also solve the thermal evolution of ambient gas simultaneously with ionization by UV radiation from

a progenitor star and discuss the effects of the thermal state of ambient gas on the evolution of the SNR. Since we are interested in low-mass star formation triggered by a supernova explosion in a very first collapsed object, we work on the conditions appropriate to such situations. The approximation and method of computations are given in § 2, and the results of our computations are presented in § 3. In § 4, we derive the conditions under which supernova explosions of first-generation stars can trigger low-mass star formation in first collapsed clouds as functions of collapse redshift and energy of the explosion. We discuss the relevance of our results in relation to the observed extremely metal-poor stars in § 5.

2. MODEL

A massive first-generation star explodes as a supernova, sweeping up the ambient medium to form an expanding gas shell. If the gas shell becomes self-gravitating, it is likely to break up into fragments, which are expected to refragment into denser cores where the next-generation stars are formed. We explore the evolution of an SNR from the expansion of a shock wave in the ambient gas to the formation of dense cores in the fragments of the swept up gas shell. The evolution of the SNR depends on two parameters: the explosion energy of the supernova, ε_0, and the density of the interstellar gas, ρ_0, in the host cloud. For given parameters, we solve the expansion and variations in the structure of the SNR by applying a semianalytical approximation to the blast wave expanding in the uniform density. The chemical compositions in the gas shell swept up by the supernova shock, which play a critical role in determining the thermal state of the SNR, are calculated by directly integrating the rate equations. To estimate the temperature and pressure in the ambient gas, we also solve the chemical and thermal evolution of the ambient gas. We describe our methods and approximations in the following subsections.

2.1. Timescales

We start by defining four typical timescales that characterize the evolution of an SNR, i.e., the expansion timescale $\tau_{\rm exp}$, the free-fall timescale $\tau_{\rm ff}$, the dynamical timescale $\tau_{\rm dyn}$, and the cooling timescale $\tau_{\rm cool}$.

The expansion timescale is defined as

$$\tau_{\rm exp} \equiv \frac{R}{\dot{R}}, \qquad (1)$$

where R and $\dot{R}$ denote the radius and the expansion speed of an SNR, respectively. The cooling timescale is given by

$$\tau_{\rm cool} \equiv \frac{nkT}{(\gamma - 1)\Lambda(T, n, \text{compositions})}, \qquad (2)$$

where T and n are the temperature and the number density in the swept up gas shell and k and γ are the Boltzmann constant and the ratio of specific heats, respectively. The symbol Λ (ergs cm^{-3} s^{-1}) denotes the total energy loss rate per unit volume, which sums up all the cooling rates that are summarized in Appendix A.

The dynamical timescale represents the time in which the sound wave crosses the gas shell as

$$\tau_{\rm dyn} \equiv \frac{\Delta R}{c_s} = \frac{R\rho_0/3\rho}{(\gamma kT/\mu m_a)^{1/2}}, \qquad (3)$$

where ρ_0 is the density of the ambient gas; ρ, c_s, ΔR and μ denote the gas density, the sound speed in the shell, the shell width, and the mean molecular weight of the shell, respectively; m_a is the atomic mass unit ($\rho = \mu m_a n$).

The free-fall timescale is written as

$$\tau_{\rm ff} \equiv \left(\frac{C}{G\rho}\right)^{1/2}, \qquad (4)$$

where G is the gravitational constant and C is a structure parameter, given by $C = 3\pi/32$ and $C = 8/\pi$ for the spherical and cylindrical collapses, respectively. Note that the free-fall timescale for the cylindrical collapse ($\tau_{\rm ff, c}$) is larger than that for the spherical collapse ($\tau_{\rm ff, s}$) by a factor of 2.94. See § 2.2 for more detail.

2.2. Expansion of SNR and Star Formation in the Fragments

In our calculation, we treat the entire evolution from expansion of the SNR shell, fragmentation of the swept up gas shell, and contraction of fragments in the expanding shell through the formation of the dense core consistently. In the following, we divide the evolution into two phases, the "antefragmentation phase" and the "postfragmentation phase" for convenience's sake. The antefragmentation phase is defined as a period in which a supernova shock propagates and gathers interstellar gas until the swept up gas shell is affected by gravitational instability and undergoes fragmentation. The postfragmentation phase is defined as a period after fragmentation occurs until the fragments contract sufficiently to become optically thick against the line emissions by H$_2$ and HD molecules.

2.2.1. The Antefragmentation Phase

Evolution of SNRs was studied extensively in the early 1970s using one-dimensional hydrodynamic codes (Cox 1972; Chevalier 1974). To summarize their results, the evolution of SNRs is divided into three stages as (1) the "free-expansion stage," (2) the "Sedov-Taylor adiabatic stage," and (3) the "pressure-driven expansion stage" (see also Ostriker & McKee 1988). As shown below, the expanding gas shell comes to be dominated by self-gravity and is expected to fragment during the pressure-driven expansion stage.

1. *The free-expansion stage* ($\tau_{\rm exp} \ll \tau_{\rm cool}$).—In this stage, the SN ejecta expand freely. After the ambient gas swept up by an SNR surpasses the SN ejecta in mass, the expansion is decelerated and the SNR enters the Sedov-Taylor adiabatic stage. With the ambient density ρ_0 and the ejecta mass $M_{\rm ej}$, the transition radius is given by

$$R_1 = (3M_{\rm ej}/4\pi\rho_0)^{1/3}. \qquad (5)$$

We put $M_{\rm ej} = 10\ M_\odot$, for simplicity. We have confirmed that the choice of the ejecta mass hardly affects the later evolution.

From comparison with the Sedov-Taylor self-similar solution (see eq. [7] below), the transition time from the free-expansion to Sedov-Taylor stages is given as

$$t_1 = \left[\frac{R_1}{1.15}\left(\frac{\rho_0}{\varepsilon_0}\right)^{1/5}\right]^{5/2} = \left[\frac{1}{1.15}\left(\frac{3M_{\rm ej}}{4\pi\rho_0}\right)^{1/3}\left(\frac{\rho_0}{\varepsilon_0}\right)^{1/5}\right]^{5/2}, \qquad (6)$$

where ε_0 represents the SN explosion energy.

2. *The Sedov-Taylor adiabatic stage* ($\tau_{exp} < \tau_{cool}$).—After the transition time t_1, the SNR is dominated by the blast wave, and hence the structure tends to a self-similar solution (Sedov 1946; Taylor 1950). The expansion of the shock front is well approximated to the Sedov-Taylor solution and described as

$$R = 1.15 \left(\frac{\varepsilon_0}{\rho_0} \right)^{1/5} t^{2/5}, \tag{7}$$

and the expansion speed of the SNR shock front is expressed by

$$V = \frac{dR}{dt} = 0.46 \left(\frac{\varepsilon_0}{\rho_0} \right)^{1/5} t^{-3/5}. \tag{8}$$

This gives the postshock pressure and shock temperature as

$$P_{ps} = 0.42 \frac{\rho_0}{(\gamma + 1)} \left(\frac{\varepsilon_0}{\rho_0} \right)^{2/5} t^{-6/5}, \tag{9}$$

$$T_{ps} = \left(\frac{8}{25} \frac{\mu m_a}{k} \right) \left(\frac{\varepsilon_0}{\rho_0} \right)^{2/5} t^{-6/5}, \tag{10}$$

respectively. These equations are derived from the Rankine-Hugoniot relation and the Sedov-Taylor solution and indicate that the postshock pressure and temperature decrease with the expansion of the SNR (Ostriker & McKee 1988; see also Sakashita & Ikeuchi 1996). The postshock gas is also cooled via radiative energy losses. Equation (2) enables us to estimate the cooling time just behind the shock front. After the cooling timescale becomes shorter than the expansion timescale, i.e., $\tau_{cool} < \tau_{exp}$, a cooled shell will form just inside the shock front and the SNR enters the pressure-driven expansion stage. We denote the time when τ_{cool} decreases to be equal to τ_{exp} by t_2.

3. *The pressure-driven expansion stage* ($\tau_{cool} < \tau_{exp}$ and $\tau_{dyn} < \tau_{ff}$).—The shell expansion is driven by the high pressure in the hot low-density cavity. The equation of motion of the shell is written as

$$\frac{4\pi\rho_0}{3} \frac{dR^3\dot{R}}{dt} = 4\pi R^2 (P_{in} - P_{hc}), \tag{11}$$

where P_{in} and P_{hc} mean the pressure in the inner cavity and the ambient gas pressure (Sakashita & Ikeuchi 1996), respectively. We assumed that the pressure inside the cavity decreases adiabatically as

$$P_{in} = P_2 \left(\frac{R}{R_2} \right)^{-3\gamma}. \tag{12}$$

In this equation, R_2 and P_2 represent the radius of the shock front and the postshock pressure, respectively, which are taken from equations (7) and (9) at the beginning of the pressure-driven expansion stage ($t = t_2$). The ambient gas pressure P_{hc} is derived by calculation of the chemical reaction and thermal evolution of ambient gas, as shown in § 2.4.

Using equation (11), we calculate the SNR expansion until fragmentation occurs in the shell (see below) or the expansion velocity of the SNR shell, V, becomes slower than the sound speed in the ambient gas of the host cloud, $c_{s,hc}$. As a result of the radiative cooling, the free-fall timescale τ_{ff} grows shorter than the sound crossing time ($\tau_{dyn} = \Delta R/c_s$) over the shell width ΔR, and the self-gravity finally becomes dominant over the pressure force in the shell. Accordingly, we may well assume

that the shell breaks into spherical fragments or cylindrical filaments when the following condition is satisfied:

$$\tau_{ff} = \tau_{dyn} \quad \text{or} \quad \Delta R = c_s \left(\frac{C}{G\rho} \right)^{1/2}. \tag{13}$$

The shell width ΔR is related to the shell density ρ as $4\pi \Delta R R^2 \rho = (4\pi/3)R^3\rho_0$, where we used the mass conservation relation. Note that this gives $\Delta R = R/12$ for the Sedov adiabatic stage if $\gamma = 5/3$. As a corollary, the above condition $\tau_{ff} = \tau_{dyn}$ is equivalent to the condition that the Jeans length in the shell is equal to the shell thickness. Such fragments produced by the breakup of the gas shell may correspond to the filamentary structures seen in the SNR, such as the Cygnus loop. Bromm et al. (2003) showed that the evolutions of SNRs of first-generation stars are well approximated by the analytical solutions used in the present paper. However, because of the restriction of numerical simulations (limited spatial resolutions), they could not explore the process after fragmentation. We solve the contraction of the fragmented pieces with a semianalytical method shown below and figure out the minimum mass of the second-generation stars.

2.2.2. *The Postfragmentation Phase*

After the gas shell fragments, each fragment piece begins to contract in a free-fall timescale. In this phase, we consider two different geometries for the fragment: the spherical and cylindrical configurations. For the spherical case, the contraction obeys the following equation:

$$\frac{dv}{dt} = -\frac{Gm_r}{r^2}, \tag{14}$$

where v and m_r represent the infall velocity and the mass contained within the radius r, respectively. For a uniform sphere, the timescale of contraction agrees with the free-fall timescale expressed by equation (4). Since the SNR shell fragments because of its self-gravity, on the other hand, the fragment is likely to have cylindrical geometry and the gas contracts in the radial direction, i.e., perpendicularly to the cylinder axis. Virial analysis of the cylindrical isothermal filament gives the equation of motion for the filament as follows:

$$\frac{dv}{dt} = -\frac{2G}{r}(\lambda - \lambda_c) \tag{15}$$

(Ostriker 1964; Uehara et al. 1996), where λ denotes the line mass of the filament [$=\pi(\Delta R/2)^2\rho$] and λ_c is the critical value corresponding to the line mass of the filament in hydrostatic equilibrium and given by

$$\lambda_c = \frac{2kT}{\mu m_a G} = \frac{2c_s^2}{G}. \tag{16}$$

This equation indicates that the line mass density must be larger than λ_c for the cylindrical fragment to contract. This condition is rewritten as

$$\tau_{dyn} > \sqrt{\frac{8}{\pi G\rho}} \equiv \tau_{ff,c} \tag{17}$$

in terms of the free-fall timescale for a cylinder with uniform density, $\tau_{ff,c} = (8/\pi G\rho)^{1/2}$ from equation (4).

As shown in the next section, the main coolants in the fragments are H_2 and HD line cooling. If the fragments are optically thick to these line emissions, the subsequent contraction proceeds nearly adiabatically, and along with the rise in the temperature, the right-hand side of equation (15) becomes no longer negative. Then the radial contraction of the fragment will be terminated, and the fragmentation is expected to occur again along the cylinder axis. Accordingly, we terminate following the contraction of the fragment when the fragments become optically thick to the line emissions of the most efficient coolant, either HD or H_2, where the optical depth is evaluated under the escape probability method. In order to estimate the optical depths of H_2 and HD lines, we use the large velocity gradient method (e.g., Goldreich & Kwan 1974). The optical depth for a transition $J + 1 \rightarrow J$ is given by

$$\tau_{J+1,J} = \frac{hc}{4\pi} \frac{B_{J,J+1} n_J}{|dv/dr|} \left(1 - \frac{g_J n_{J+1}}{g_{J+1} n_J}\right), \tag{18}$$

where h is Planck's constant, c is the speed of light, $B_{J,J+1}$ is the Einstein B-coefficient, and n_J and g_J are the number density and statistical weight of the Jth level, respectively. The number density of the Jth level is evaluated using a two-level transition model with fitting formulas of the collisional deexcitation rates by Galli & Palla (1998) and Flower & Roueff (1999). The first six rotational transition levels are taken into account. The velocity gradient, $|dv/dr|$, is approximated as $\alpha v_{th}/R_J = \alpha(\pi G\rho)^{1/2}$, where α, v_{th}, and R_J are a nondimensional numerical constant, the thermal velocity of HD, and the filament radius, respectively. The value of α depends on the velocity distribution of the collapsing filament. When the density reaches a critical density of HD cooling, the contraction of the filament becomes quasi-static, and therefore the velocity gradient becomes subsonic (Nakamura & Umemura 2002b). We thus set α to unity, for simplicity.

It is thought that the Jeans mass, when the fragment becomes optically thick against the line emissions of the most efficient coolant (H_2 or HD), gives the characteristic minimum mass for stars that will be formed in the fragment pieces, and hence, if it is much smaller than $\sim 0.8\, M_\odot$, we may well expect that the low-mass stars surviving today can be formed. For respective stages, we study the thermal and chemical histories of the SNR shell with a one-zone approximation, which is explained below.

2.3. Temperature and Density in the Shell

2.3.1. The Antefragmentation Phase

The temperature at the transition epoch, t_1, from the free-expansion to the Sedov-Taylor adiabatic stage is determined from the condition that the transition is continuous as

$$T(t_1) = (1.15)^5 \frac{\pi}{25} \frac{\mu m_a}{k} \frac{\varepsilon_0}{M_{ej}} \tag{19}$$

with $\gamma = 5/3$. We calculate the variation in the temperature of the shell under the one-zone approximation in the following way:

$$\frac{dT}{dt} = \left(\frac{dT}{dt}\right)_{exp} + \left(\frac{dT}{dt}\right)_{rad} + \left(\frac{dT}{dt}\right)_{comp}, \tag{20}$$

where $(dT/dt)_{exp}$, $(dT/dt)_{rad}$, and $(dT/dt)_{comp}$ represent the terms due to the expansion cooling, the radiative cooling, and the

compressional heating due to contraction of the shell, respectively. In the Sedov-Taylor adiabatic stage, the postshock temperature is given by the similarity solution, where $T \propto t^{-6/5}$. Thus, the expansion cooling term is denoted as

$$\left(\frac{dT}{dt}\right)_{exp} = -1.2 \frac{T}{t}. \tag{21}$$

This term is only effective in the Sedov-Taylor adiabatic stage, and in the pressure-driven expansion stage it tends to be negligible as compared with the radiative cooling and the compressional heating term. Thus, we include the expansion cooling only in the Sedov-Taylor stage and ignore it after the pressure-driven stage.

The radiative cooling term is denoted as

$$\left(\frac{dT}{dt}\right)_{rad} = -\frac{T}{\tau_{cool}} = -T\frac{(\gamma - 1)\Lambda(T, n, \text{composition})}{P}. \tag{22}$$

In this cooling, we include the inverse Compton cooling (Ikeuchi & Ostriker 1986) and the radiative cooling by the atoms and ions of H and He (Cen 1992) and by H_2 and HD molecules (Galli & Palla 1998; Flower et al. 2000). We take into account the effect of the cosmic microwave background (CMB) radiation on the radiative cooling by modifying the total cooling rate as

$$\Lambda = \Lambda(T) - \Lambda(T_{CMB}), \tag{23}$$

where the cosmic background temperature T_{CMB} is calculated as $T_{CMB} = 2.73(1 + z)$ K. Owing to this formula, the gas cannot cool below the CMB temperature at that time.

The compressional heating has a form

$$\left(\frac{dT}{dt}\right)_{ad} = (\gamma - 1)\frac{T}{n}\frac{dn}{dt}, \tag{24}$$

where n represents the number density of molecules, atoms, ions, and electrons. This term becomes effective after the shell has cooled and the density increases.

The density in the shell is given by the jump condition across the strong shock front during the Sedov-Taylor stage as

$$\rho = \frac{\gamma + 1}{\gamma - 1} \rho_0, \tag{25}$$

where ρ_0 represents the ambient gas density. This equation indicates that the density in the shell is equal to $4\rho_0$ for $\gamma = 5/3$. After the condition $\tau_{cool} < \tau_{exp}$ is realized in the pressure-driven stage, the time evolution of physical quantities in the shell differs according to whether the cooling time is shorter than the sound crossing time of the shell ($\tau_{cool} < \tau_{dyn}$) or the other way around ($\tau_{dyn} < \tau_{cool}$). In the former case, the shell cools without changing the width of the shell. Thus, we assume

$$\frac{d\rho}{dt} = 0, \quad \text{for} \quad \tau_{cool} < \tau_{dyn}. \tag{26}$$

Accordingly, the pressure in the shell varies in proportion to the temperature given by equation (20) in this regime.

If the sound crossing time is shorter than the cooling time ($\tau_{dyn} < \tau_{cool}$), on the other hand, the shell is subject to compression, and in the decelerating frame with the gas shell, the

structure tends to be in hydrostatic equilibrium with the boundary pressures given by the inner cavity pressure (eq. [12]) and the postshock pressure, P_{out}. Thus, we assume that the pressure in the shell is brought near to the average of P_{in} and P_{out} in a dynamical timescale as follows:

$$\frac{dP}{dt} = \left(\frac{P_{\mathrm{in}} + P_{\mathrm{out}}}{2} - P\right)\frac{1}{\tau_{\mathrm{dyn}}}, \quad \text{for} \quad \tau_{\mathrm{dyn}} < \tau_{\mathrm{cool}}, \quad (27)$$

where the postshock pressure is assumed as the sum of the ram pressure and the pressure in the ambient gas P_{hc}:

$$P_{\mathrm{out}} = \frac{2}{\gamma + 1}\rho_0 \dot{R}^2 + P_{\mathrm{hc}}. \quad (28)$$

The density variation at this stage is determined by equations (20) and (27) with the equation of state.

2.3.2. *The Postfragmentation Phase*

During the pressure-driven expansion stage, the dynamical timescale lengthens as the shell expands, eventually reaching the free-fall timescale. When the condition $\tau_{\mathrm{ff}} < \tau_{\mathrm{dyn}}$ is satisfied, the shell begins to fragment owing to self-gravity, and the evolution enters the final stage of the fragmentation and star formation stage. As mentioned above, the subsequent evolution of the fragments seems to differ according to their geometry. We consider two different types of fragment geometry, i.e., the spherical and the cylindrical symmetric configurations. For spherical fragments, the time variation of the density is approximated as

$$\frac{d\rho}{dt} = \frac{\rho}{\tau_{\mathrm{ff},s}} \quad (29)$$

with the free-fall timescale given by equation (4).

On the other hand, if the fragments form long cylindrical shapes, the widths of the filaments shrink with time according to equation (15). Since equation (15) gives the contraction timescale of $\simeq r/[2G(\lambda - \lambda_c)]^{1/2} \simeq 1/[2\pi G\rho(1 - \lambda_c/\lambda)]^{1/2}$, we assume that the density changes as

$$\frac{d\rho}{dt} = \frac{\rho}{\tau_{\mathrm{ff},c}(\rho)}\left(1 - \frac{\lambda_c}{\lambda}\right)^{1/2}, \quad (\lambda > \lambda_c) \quad (30)$$

with the line mass density λ determined at the fragmentation (Ostriker 1964).

The cylindrical collapse proceeds much more slowly than the spherical collapse (Uehara et al. 1996). This comes from the factor $1 - \lambda_c/\lambda$ in equations (15) and (30). Along with the cooling of the gas, λ_c decreases. If the critical line mass λ_c becomes smaller than the line mass, i.e., $\lambda > \lambda_c$, the filament contracts. At the same time, the contraction causes λ_c to increase because of the compressional heating. If λ_c increases to approach λ, the contraction slows down, and it finally halts when λ_c reaches λ. Accordingly, the contraction of filaments proceeds in the cooling timescale, keeping the temperature slightly lower than determined from the condition $\lambda_c = \lambda$, and hence much more slowly than in the free-fall timescale. This makes a clear contrast to the fast collapse accomplished for the spherical system (eq. [29]).

In our calculation, the initial line mass λ is determined at the fragmentation epoch ($\tau_{\mathrm{ff}} = \tau_{\mathrm{dyn}}$) under the assumption that

fragmentation occurs with a wavelength equal to the shell width. This gives a line mass of

$$\lambda = \pi\left(\frac{\Delta R}{2}\right)^2 \rho = \frac{\pi R^2 \rho_0^2}{36\rho}, \quad (31)$$

where we used the shell thickness of $\Delta R = \rho_0 R/3\rho$. As the shell expands, the fragments accumulate additional gas that is swept up by the shell. We assume that the line mass increases in proportion to the shell mass as

$$\frac{d\lambda}{dt} = \lambda\frac{\dot{M}_{\mathrm{sw}}}{M_{\mathrm{sw}}}, \quad (32)$$

where M_{sw} and $\dot{M}_{\mathrm{sw}}$ represent the shell mass and the rate of increase in the shell mass, respectively. Along with the increase in λ, the contraction becomes shorter than the expansion, and thereafter λ stays constant, since the contraction is further accelerated with the decrease in the free-fall and cooling timescales with the increases in the density. We also assume that the mass of the spherical fragments increases in proportion to the shell mass. However, since the spherical collapse is much faster than the cylindrical one, this does not play an important role.

2.4. *The Evolution of the Ambient Gas*

The thermal state of the ambient gas may play a part in the evolution of the expanding gas shell in the pressure-driven expansion phase (§ 2.2.1, stage 3) and the resultant fragmentation of the swept up shell. In the course of the formation of first-generation stars, gas in the primordial clouds suffers cooling by H_2 molecules formed with relic electrons as agents, and the gas temperature can decrease as low as $\sim$200 K (e.g., Bromm et al. 2002). Once a massive star is born, however, gas is ionized by the radiation of the massive progenitor stars and heated to $T \sim 10^4$ K. After the massive star explodes, radiation coming from the interior of the SNR may heat the ambient gas or destroy the hydrogen molecules.

As for the UV radiation from a progenitor star, the extent of the ionized region depends on the ratio of the total number of ionization photons per unit time to the recombination rate of the hydrogen. If we assume an O5-type progenitor star and the ambient gas density of $n_0 = 1$ cm^{-3}, this star ionizes the ambient gas inside the Strömgren radius of $\simeq$100 pc (Panagia 1973). After the massive star explodes, the ambient ionized gas begins to recombine. Although the ambient gas continues to cool by radiative cooling, the gas near the shock front (preshock gas) may be heated by the ionization radiation from the SNR's hot interior (Shelton 1999; Slavin et al. 2000).

The preshock gas ionized by the radiation emitted from the postshock hot gas is calculated by Shull & McKee (1979) for a metal-rich gas cloud and by Shull & Silk (1979) for a metal-poor gas cloud. The controlling parameter for this problem is the ratio of the emergent photon flux Φ (cm^{-2} s^{-1}) from the postshock gas to the hydrogen atom number flux $n_0 V$ (cm^{-2} s^{-1}) flowing into the SNR. Shull & Silk (1979) showed that the emitted photons scarcely ionize the ambient gas for $n_0 = 1$ cm^{-3} if the shock velocity is as low as $V \lesssim 60$ km s^{-1} because the above photon-to-gas ratio $\Phi/n_0 V \ll 1$ is too small at that time. Thus, the heating of the preshock gas by the SNR shock is negligible in the late evolutionary phase ($V \lesssim 60$ km s^{-1}). In the early evolutionary phase, the emission from the SNR shock is also negligible because the shock is strong and the ambient gas pressure does not play a role, as discussed in Shapiro & Kang (1987).

In our calculation, as long as the shock speed is faster than $V > 60$ km s^{-1}, the ionization level of the ambient gas is always much higher than that expected from the ionization by the SNR (Shull & McKee 1979) and its temperature is maintained at $T_{\rm hc} \sim 10^4$ K because the ambient gas photoionized by the progenitor star has not recombined/cooled sufficiently by this epoch. Thus, we expect that SNR evolution is not affected, whether the ionizing photons emitted from the SNR are considered or not. Therefore, we neglect ionization by the ionization photons from the SNR.

The SNR radiation may prevent the ambient gas from cooling through the dissociation of the H$_2$ molecules, which is the effective coolant at lower temperature ($T < 10^4$ K). The dissociation timescale of the molecular hydrogen, $t_{\rm dis}$, is given by $t_{\rm dis} = 2.8 \times 10^{-16} F_{\rm LW}^{-1}$ yr (Omukai & Nishi 1999). Here $F_{\rm LW}$ (ergs s^{-1} cm^{-2} Hz^{-1}) is the average radiation flux in the Lyman-Werner (LW) bands. The flux $F_{\rm LW}$ is estimated as a function of the shock velocity of the SNR (Shull & McKee 1979; Shull & Silk 1979). The hydrogen molecules begin to form after the shock velocity decelerates below $V = 60$ km s^{-1} in our calculation. From the flux $F_{\rm LW} \simeq 1.3 \times 10^{-22}$ ergs s^{-1} cm^{-2} Hz^{-1} for $n_0 = 1$ cm^{-3} at the stage of $V = 60$ km s^{-1} (Shull & Silk 1979), the dissociation timescale is given as $t_{\rm dis} = 2.2 \times 10^6$ yr, which is much longer than the formation timescale of the molecular hydrogen, $n_{\rm H_2}/(dn_{\rm H_2}/dt)$. After that, the dissociation timescale continues to increase because the flux $F_{\rm LW}$ decreases with time, and it stays longer than the formation timescale. Therefore, radiation from an SNR barely decreases the molecular fraction of ambient gas.

As a result, we can safely ignore the effect of radiation from hot gas in the SNR and include only the effects of photoionization and heating due to the progenitor star. However, the above effect may delay the cooling of the ambient gas slightly. In § 4, we discuss how the expansion of the shell is affected if we assume a higher temperature ambient gas than that calculated in § 3 and show the condition for low-mass star formation.

In order to obtain the proper boundary conditions of SNR shell evolution, we need to know the evolution of the ambient pressure. For this reason, we solve the chemical reactions and the thermal evolution of the ambient gas simultaneously with the dynamical and thermal evolution of the SNR shell. The initial chemical composition of the ambient gas is derived under the assumption that the ambient gas has been heated and is kept at a temperature of $T_{\rm hc} = 10^4$ K by the progenitor star of the first generation that lives for 10^6 yr. After the progenitor star explodes, we assume that the heating source disappears and follow the cooling of the ambient gas by solving the same rate equations and the equation of energy conservation, as described above, under the constant density of ρ_0. From the ambient temperature, $T_{\rm hc}$, we derive the interstellar pressure $P_{\rm hc}$ by

$$P_{\rm hc} = \frac{\rho_0 k}{\mu_{\rm hc} m_a} T_{\rm hc}, \qquad (33)$$

where $\mu_{\rm hc}$ is the mean molecular weight of the ambient gas. This pressure is applied to the evolution of the SNR gas shell in equation (11). The SNR shell can continue expanding and sweeping up the ambient gas only when the expansion speed is faster than the sound speed as

$$V > c_{s,\rm hc}. \qquad (34)$$

Otherwise ($V < c_{s,\rm hc}$), the gas shell dissolves and merges into the ambient gas. Accordingly, the above condition (eq. [34]) has to be satisfied for the gas shell to fragment.

2.5. Chemical Composition

We have modeled the thermal and dynamical evolution of the SNR shell and ambient medium under the one-zone approximation, as stated above. The cooling rates in the gas shell and ambient medium are determined by their chemical composition. To estimate the abundances of chemical species in these gases, we solve the time-dependent chemical reaction equations numerically. In this paper, we consider the chemical reactions of the following 12 species: H, H$^+$, H$^-$, He, He$^+$, He^{++}, H$_2$, D, D$^+$, HD, HD$^+$, and e^-, as shown in Table 2. We adopt the primordial composition obtained by Galli & Palla (1998) as the initial condition of our calculations. The reaction rates that we include in our calculations are summarized in Appendix B.

3. RESULTS

We begin our computation from the transition epoch, t_1, between the free-expansion and the Sedov-Taylor adiabatic stages given by equation (6) for a given set of values of the explosion energy, ε_0, and the density, ρ_0, of the host cloud. Then we solve the equations of structural changes in the expanding SNR and the rate equations for the changes in the chemical abundances formulated in the preceding section. In this work, we adopt an explosion energy between $\varepsilon_0 = 10^{51}$ and 10^{52} ergs, ranging from a normal supernova to a hypernova (Nomoto et al. 1999). The density of interstellar gas in the host cloud is taken to be in the range between $\rho_0 = 3.51 \times 10^{-25}$ and 3.49×10^{-23} g cm^{-3}, taking into account the formation epoch of the host clouds. Since the densities in the virialized host clouds are approximated to 200 times the average baryon density in the universe at that epoch (White et al. 1993), the above density range corresponds to the redshifts of formation epoch $z = 10 - 50$ for the Einstein–de Sitter universe model [$\rho_0 \propto (1 + z)^3$] with a Hubble constant of $H_0 = 70$ km s^{-1} Mpc^{-1} and baryon fraction of $\Omega_B = 0.06$.

The model parameters adopted are listed in Table 1 with the characteristic physical quantities of gas shells and ambient gas when the condition of fragmentation, $\tau_{\rm ff} = \tau_{\rm dyn}$, is fulfilled. In the following, we discuss the results, dividing the evolution into two phases, defined in the preceding section: the antefragmentation phase ($\tau_{\rm ff} > \tau_{\rm dyn}$) until the gas shell undergoes fragmentation and the postfragmentation phase ($\tau_{\rm ff} < \tau_{\rm dyn}$) during which the fragments collapse gravitationally, eventually forming second-generation stars.

3.1. The Antefragmentation Phase

Figure 1 shows the evolution of the shell radius and the expansion velocity of the SNR against the elapsed time from the SN explosion for various models. For each model, the expansion of the SNR is well expressed by two power laws, in which the break occurs at the transition time t_2 from the Sedov-Taylor ($R \propto t^{2/5}$; eq. [7]) to the pressure-driven stages ($R \propto t^{2/7}$; eq. [11]). The expansion velocity and, hence, the radius of the SNR are larger for smaller collapse redshifts and for larger explosion energy. For example, the initial radius at the transition epoch $t_1 = 2.1 \times 10^3$ yr for $z = 10$ is 4.7 times as large as that at $t_1 = 2.6 \times 10^2$ yr for $z = 50$. We note that the expansion velocity and radius depend weakly on ambient density, as inferred from the Sedov-Taylor similarity solution [$R \propto (\varepsilon_0/\rho_0)^{1/5}$], but the ambient density depends strongly on the collapse redshift

TABLE 1
INITIAL CONDITIONS AND RESULTS

Model (1)	ε_0 (10^{51} ergs) (2)	z (3)	ρ_0 (10^{-25} g cm^{-3}) (4)	t_f (Myr) (5)	r (pc) (6)	V (km s^{-1}) (7)	V_{esc} (km s^{-1}) (8)	M_{sw} ($10^4 M_\odot$) (9)	T (K) (10)	T_{hc} (K) (11)	$c_{s,hc}$ (km s^{-1}) (12)	[H$_2$/H] (log 10) (13)	[HD/H] (log 10) (14)
A10..................	1	10	3.51	45.4	198	1.17	11.1	17.1	32	277	1.89	−2.72	−4.75
B10..................	3	10	3.51	38.7	251	1.78	14.1	34.9	36	303	1.98	−2.73	−4.83
C10..................	5	10	3.51	36.9	281	2.12	15.8	49.0	70	311	2.01	−2.79	−5.11
D10..................	10	10	3.51	36.6	332	2.61	18.6	80.4	98	312	2.01	−2.83	−5.41
A20..................	1	20	24.4	14.7	90	1.73	13.2	11.1	53	223	1.70	−2.80	−5.08
B20..................	3	20	24.4	12.2	111	2.43	16.4	20.8	69	248	1.83	−2.80	−5.20
C20..................	5	20	24.4	10.9	122	2.99	17.9	27.4	83	262	1.85	−2.80	−5.29
D20..................	10	20	24.4	10.9	137	3.94	20.2	39.2	109	282	1.91	−2.81	−5.46
A30..................	1	30	78.5	8.42	56	1.75	14.9	8.75	75	199	1.61	−2.78	−5.01
B30..................	3	30	78.5	6.55	68	2.49	18.1	15.6	79	228	1.72	−2.78	−5.09
C30..................	5	30	78.5	4.73	70	4.04	18.6	16.9	87	278	1.91	−2.78	−5.26
D30..................	10	30	78.5	3.79	77	5.62	20.3	22.3	120	321	2.04	−2.78	−5.51
A40..................	1	40	182	5.85	40	1.85	16.0	7.16	99	194	1.54	−2.76	−5.17
B40..................	3	40	182	5.10	49	2.51	20.3	14.3	102	207	1.64	−2.76	−5.19
C40..................	5	40	182	3.17	50	4.04	20.3	14.4	108	276	1.89	−2.76	−5.28
D40..................	10	40	182	1.57	51	9.02	20.2	14.5	151	656	2.92	−2.77	−5.73
A50..................	1	50	349	4.40	30	1.97	17.0	6.07	124	193	1.58	−2.73	−5.40
B50..................	3	50	349	3.82	38	2.52	21.4	12.2	127	206	1.64	−2.74	−5.42
C50..................	5	50	349	2.73	39	4.18	21.6	12.7	132	260	1.84	−2.74	−5.46
D50..................	10	50	349	1.08	39	9.09	21.6	12.7	154	567	2.71	−2.74	−5.66

NOTES.—Symbols t_f, r, V, V_{esc}, M_{sw}, T, T_{hc}, $c_{s,hc}$, [H$_2$/HD], and [HD/H] represent the elapsed time, the radius of the shell, the expansion speed, the escape velocity, the swept up mass, temperature of the shell, temperature of the ambient medium, sound speed of the ambient medium, and H$_2$ and HD fractional abundances in the logarithmic scale, respectively.
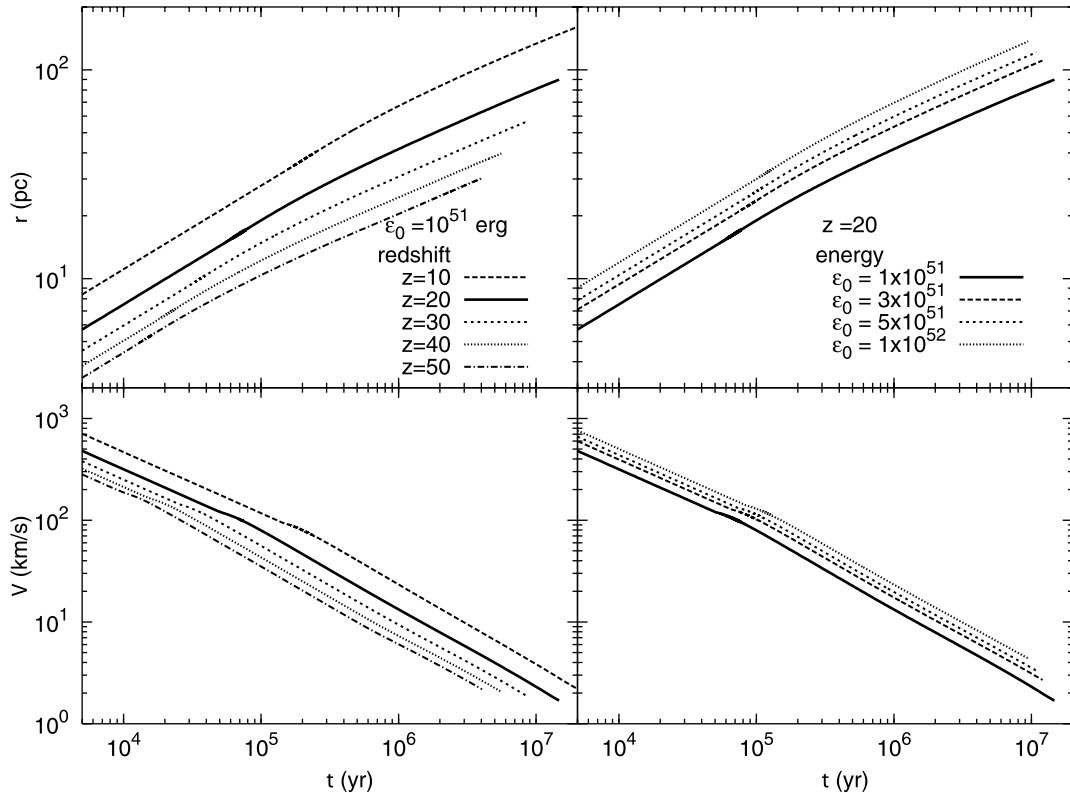

FIG. 1.—Evolution of SNR radius (*top*) and shell expansion velocity (*bottom*) compared among the models of different ambient densities ($z = 10$, 20, 30, 40, and 50) but a fixed explosion energy ($\varepsilon_0 = 10^{51}$ ergs; *left*) and among the models of different explosion energies ($\varepsilon_0 = 1$, 3, 5, and 10×10^{51} ergs) but a fixed ambient density ($z = 20$; *right*). [*See the electronic edition of the Journal for a color version of this figure.*]
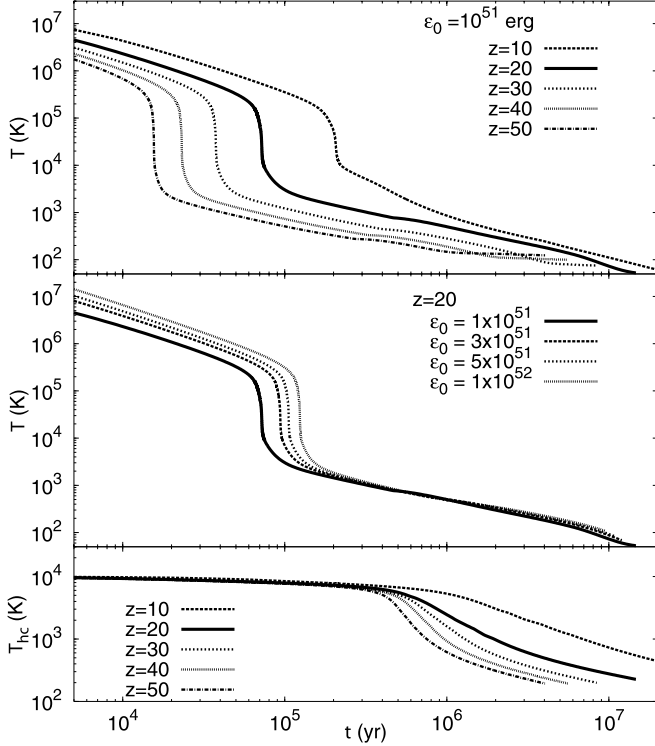
FIG. 2.—Time variations in the temperature of the gas shell (*top and middle*) and that of the ambient gas (*bottom*) vs. elapsed time. In the top and bottom panels, models with different ambient densities (or different redshifts of formation of the host cloud $z = 10, 20, 30, 40,$ and 50) but a fixed explosion energy ($\varepsilon_0 = 10^{51}$ ergs), are compared. The middle panel compares the models with different explosion energies ($\varepsilon_0 = 1, 3, 5,$ and 10×10^{51} ergs) but a fixed ambient density (or redshift $z = 20$). [*See the electronic edition of the Journal for a color version of this figure.*]

FIG. 3.—Variations of the pressures of the swept up gas, P, the cavity gas, P_{in}, the postshock gas, P_{out}, and the ambient gas, P_{hc}. Model A20 of $(z, \varepsilon_0) = (20, 10^{51}$ ergs) is shown for the antefragmentation phase. [*See the electronic edition of the Journal for a color version of this figure.*]

$[\rho \propto (1 + z)^2]$. Therefore, the expansion velocity and radius change greatly with z. More quantitative results of all models are summarized in Table 1.

The evolutionary variations of thermal state in the swept up gas shell and ambient gas are shown in Figures 2, 3, and 4 as a function of elapsed time. Figure 2 shows the temperature variations of the gas shell (*top and middle panels*) and ambient gas (*bottom panel*) for models with different redshifts (*top and bottom panels*) and for different explosion energies (*middle panel*). The temperature of the SNR shell (*top and middle panels*) decreases gradually with expansion during the Sedov-Taylor adiabatic stage. The initial temperature is determined from the energy conservation at transition time t_1 in equation (19). The temperature steeply descends from $T \simeq 10^5$ to 10^4 K owing to efficient atomic cooling by He and H (see Fig. 7, *left*). As the temperature decreases below 10^4 K, the temperature drop slows again and yet continues to decrease below 100 K owing to cooling by H_2 molecules and then by HD molecules. There are two small dents discernible around $T \simeq 10^3$ and 150 K, which are caused by the cooling due to H_2 and HD molecules, respectively. For higher redshifts, the temperature decreases to the CMB temperature. For $\varepsilon_0 = 10^{51}$ ergs models, this occurs for $z \gtrsim 30$, and then the SNRs evolve isothermally, as seen in Figure 2 (*top*; at $t \gtrsim 10^6$ yr). For the larger explosion energy, however, the gas shell sweeps up the ambient gas at a higher rate because of larger expansion velocity and hence can satisfy the condition for fragmentation at higher temperatures before it cools to the CMB temperature even for the largest redshift $z = 50$ as seen from the $\varepsilon_0 \geq 1 \times 10^{52}$ ergs models.
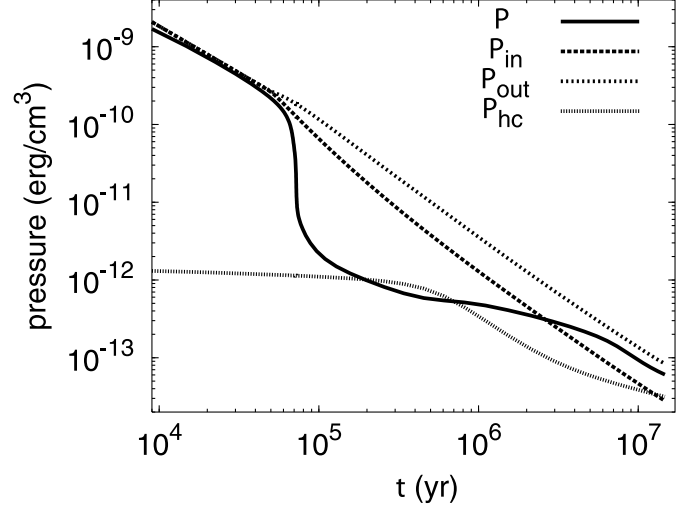
Since the radiative cooling is in proportion to the density squared, the cooling is faster for models with larger ambient densities (or larger redshifts). Accordingly, the time interval from the supernova explosion to the shell fragmentation epoch is shorter for larger ambient gas density or for larger redshifts of the host cloud collapse, decreasing by a factor of 10–30 from several times 10^7 yr to $\sim 10^6$ yr between $z = 10$ and 50. If the ambient gas density is the same, the model with smaller explosion energy has an earlier onset of rapid atomic cooling. After the gas cools to $T \lesssim 10^3$ K, the evolution converges because of the strong temperature dependence on atomic cooling. Accordingly, the time interval from supernova explosion to fragmentation is elongated for a smaller explosion energy, since it takes longer to gather the necessary mass because of smaller expansion velocity.

In Figure 2 (*bottom*), we show the evolutions of the temperature, T_{hc}, in the ambient gas for several different values of collapse redshift z. The ambient gas evolves almost isothermally for $t \simeq 4 \times 10^5$ to 10^6 yr, and then the temperature decreases below $T_{hc} = 1000$ K for 10^6–10^7 yr. For the model with $z = 20$ and $\varepsilon_0 = 10^{51}$ ergs, the temperature of the ambient gas decreases to $T_{hc} = 223$ K in 14.7 Myr by the time the temperature of the SNR shell decreases to $T = 53$ K and satisfies the conditions of fragmentation. The cooling of the ambient gas is also faster for models with higher redshifts because of the higher density of the ambient gas. The ambient gas can finally cool to the temperature range of $T_{hc} = 193$–656 K when the condition for fragmentation is satisfied, as listed in Table 1, column (11), with the sound speed, $c_{s,hc}$, in column (12).

Figure 3 illustrates the time variations in the pressure in the gas shell, P, along with those of the boundary pressures, i.e., the cavity pressure inside the gas shell P_{in} (eq. [12]) and the postshock pressure outside the gas shell P_{out} (eq. [28]) for the model with $z = 20$ and $\varepsilon_0 = 10^{51}$ ergs. As the atomic cooling becomes very effective in the pressure-driven stage, the pressure in the shell starts to decrease nearly in proportion to the temperature in the gas shell, since $\tau_{cool} \ll \tau_{dyn}$; hence, the dynamical readjustment of structure cannot catch up with the temperature drop caused by the radiative cooling. The radiative cooling rate declines very steeply below 10^4 K. As the cooling timescale grows longer and eventually exceeds the dynamical timescale ($\tau_{dyn} \ll \tau_{cool}$), the gas shell starts to readjust its structure to the surrounding
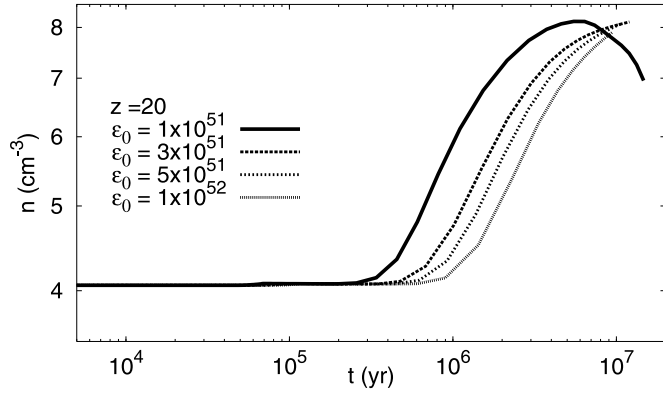
FIG. 4.—Time variations in the number density of gas in the gas shell for models with different energies ($\varepsilon_0 = 1$, 3, 5, and 10×10^{51} ergs) but a fixed redshift of $z = 20$. [*See the electronic edition of the Journal for a color version of this figure.*]

pressures, and the pressure approaches the average of P_{in} and P_{out} according to equation (27). In particular, for $t \gtrsim 10^6$ yr, when the time grows longer than τ_{dyn}, the gas shell restores the adjustment and the pressure P tends to be controlled by the boundary pressures and decreases with them.

In this figure, we also plot the ambient pressure P_{hc}. The ambient pressure remains much lower than the inner pressure, P_{in}, for most of the time, and it is only after $t > 1.3 \times 10^7$ yr that the ambient pressure grows higher than the inner pressure. Since their difference attains only 9% at the time of fragmentation and is much smaller than the momentum flux of the gas shell, the effect of decelerating the expansion of the SNR shells is rather small and hence will not affect the evolution of the SNR shell so much. In this model, the SNR gas shell keeps expanding at a velocity exceeding the sound speed and hence undergoes fragmentation without dissolving and merging into the ambient gas. For the models of larger explosion energy and higher ambient density, the condition that $V > c_{s,hc}$ holds by a greater margin because of greater expansion velocity at the time of fragmentation, as seen from Table 1.

The changes in the number density in the gas shell are plotted in Figure 4. The gas density in the shell is kept nearly constant at $4\rho_0$ until τ_{dyn} becomes shorter than τ_{cool} at $t \gtrsim 3 \times 10^5$ yr and for $T \lesssim 10^4$ K. Then the density starts to increase as the gas shell undergoes compression by the pressures at the inner and outer boundaries. Finally, when the gas shell restores the hydrostatic equilibrium, the density begins to decrease along with the boundary pressures that confine the gas shell, as seen from the model with the smallest explosion energy. For the greater explosion energy, however, this final stage does not occur; because of greater expansion velocity, the SNR gathers more gas to make the shell thicker and the dynamical timescale longer in proportion; hence, the fragmentation condition is satisfied before the hydrostatic equilibrium is restored.

We show examples of the behaviors of the four timescales mentioned above in Figure 5, which shows the evolutionary changes in the expansion time, the cooling time, the dynamical time, and the free-fall time for three models of $(z, \varepsilon_0) = (20, 10^{51}$ ergs) (Fig. 5a), (50, 10^{51} ergs) (Fig. 5b), and (20, 10^{52} ergs) (Fig. 5c). As the temperature descends to $T \simeq 10^5$ K, τ_{cool} starts to decline rapidly owing to atomic cooling and eventually becomes shorter than the expansion timescale τ_{exp}, which increases with time. This causes a transition from the Sedov-Taylor adiabatic stage to the pressure-driven stage. When the temperature falls further to $T \simeq 2 \times 10^4$ K, τ_{cool} reverses the direction of the change and begins to increase. As the recombination of hydrogen atoms proceeds with a further drop in the temperature, τ_{cool} grows large very rapidly, increasing by a factor of ~ 100 while the temperature decreases to $T \simeq 5 \times 10^3$ K, and forms a sharp minimum. Thereafter, the cooling timescale continues to increase constantly, slowing the increase rate slightly by the enhancement of cooling by H_2 and HD molecules (two small dents are discernible at $t \simeq 5 \times 10^5$ and 5×10^6 yr; Fig. 5a). On the other hand, the dynamical timescale grows large owing to both the decrease in the temperature and the increase in the shell thickness. Therefore, when the atomic cooling begins to be effective, the cooling timescale becomes smaller than the dynamical timescale. As the temperature decreases below 10^4 K, they reverse their relation and the cooling timescale grows larger than the dynamical timescale
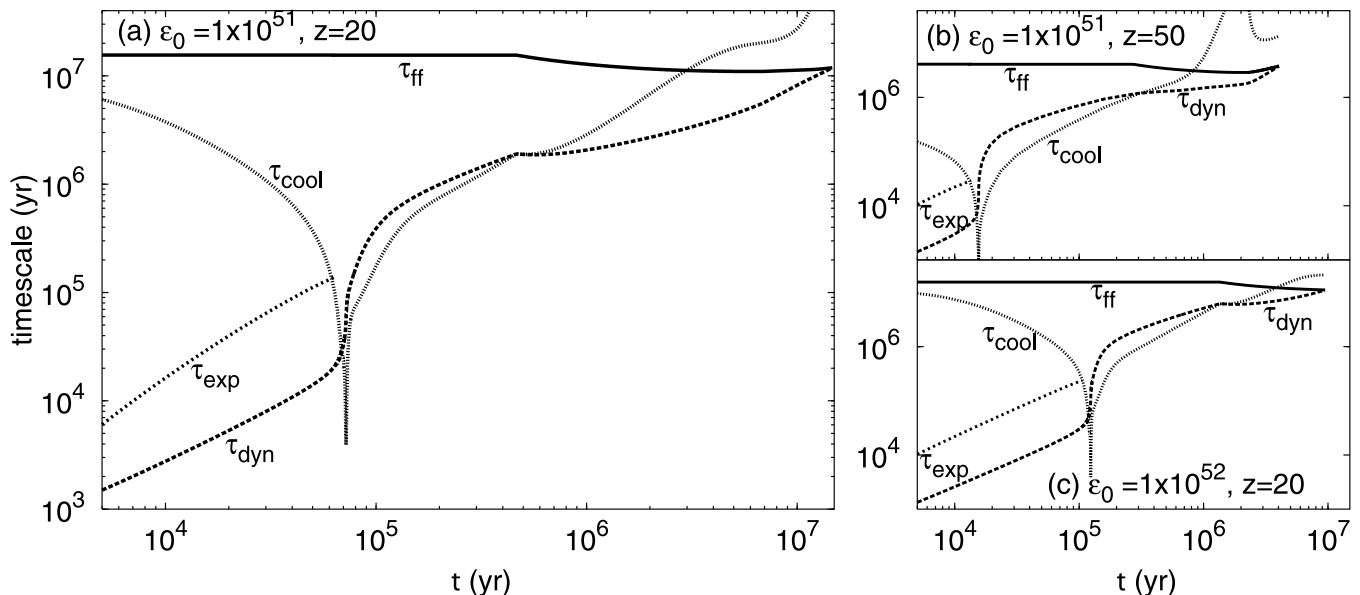

FIG. 5.—Evolutions of four typical timescales (τ_{ff}: free-fall timescale, τ_{dyn}: dynamical timescale, τ_{exp}: expansion timescale, and τ_{cool}: cooling timescale) vs. elapsed time. (a) Model with $(z, \varepsilon_0) = (20, 1 \times 10^{51}$ ergs); (b) model with $(z, \varepsilon_0) = (50, 1 \times 10^{51}$ ergs); (c) model with $(z, \varepsilon_0) = (20, 5 \times 10^{51}$ ergs). We show τ_{exp} only for the Sedov-Taylor stage. [*See the electronic edition of the Journal for a color version of this figure.*]
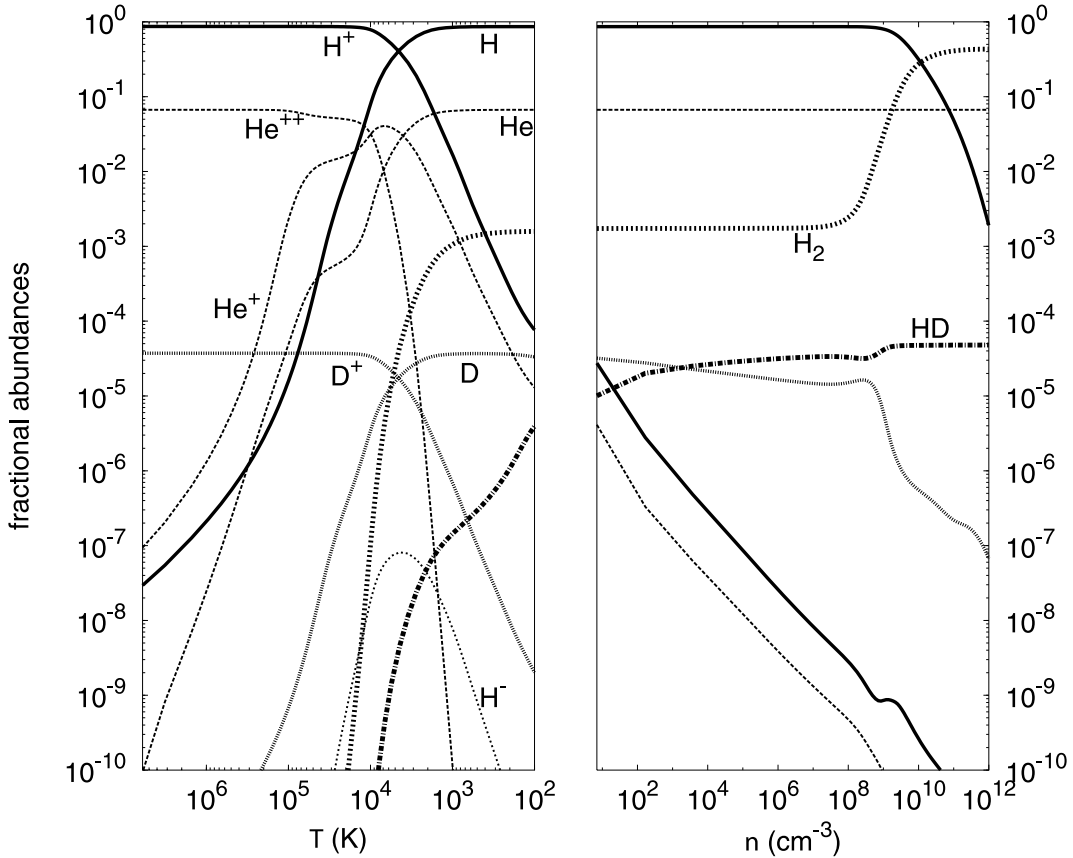
FIG. 6.—Time variations in the fractional abundances for 10 species (H, H$^+$, H$^-$, H$_2$, He, He$^+$, He^{++}, HD, D, and D$^+$) in the gas shell for the model with $\varepsilon_0 = 10^{51}$ ergs and $z = 20$. The abundance is plotted as a function of temperature (*left*) before the fragmentation and as a function of number density (*right*) after the fragmentation. In the postfragmentation phase, we assume that a cylindrical fragment contracts in the radial direction. [*See the electronic edition of the Journal for a color version of this figure.*]

again. When $\tau_{dyn} \lesssim \tau_{cool}$, the gas shell undergoes compression, as seen above. Then the density in the shell increases, which causes a decrease in the free-fall timescale, as seen from $t \gtrsim 5 \times 10^5$ yr, while the dynamical timescale continues to increase because of the decrease in the shell temperature and also because of the increase in the shell thickness. Finally, τ_{ff} becomes as short as τ_{dyn} ($t \simeq 10^7$ yr for Fig. 5*a*), and the gas shell is expected to break up into fragments, each of which undergoes gravitational contraction.

For higher ambient density (or higher z; Fig. 5*b*), the cooling, dynamical, and free-fall timescales are shorter, while the expansion timescale is slightly dependent on the density in the gas shell. These accelerate the evolution. Accordingly, the fragmentation epoch comes earlier because the gas in the shell cools more rapidly and the free-fall timescale is smaller for higher density. For the model with greater explosion energy (Fig. 5*c*), the temperature remains higher, which delays transition to the pressure-driven stage. In the later stage, the difference in the temperature tends to be eliminated as a result of the atomic cooling. On the other hand, faster expansion makes the shell thicker and the dynamical timescale longer. This delays the arrival of the epoch of $\tau_{cool} > \tau_{dyn}$ and the contraction of the gas shell, as seen in Figure 4, but brings forward the epoch of fragmentation slightly. Accordingly, we conclude that the time necessary for fragmentation depends significantly on the ambient gas density (ρ_0 or the formation redshift z) but weakly on the explosion energy (ε_0).

We present typical patterns of the evolution of fractional abundances and of the variations in the cooling rates against the shell temperature, T, in the left panels of Figures 6 and 7, respectively,

for the $(z, \varepsilon_0) = (20, 10^{51}$ ergs) model. The ambient gas is ionized by the SNR shock at first and then recombines around $T \simeq 5 \times 10^3$ K. Thereafter, H$_2$ and HD molecules are formed through the reactions as

$$e^- + H \rightarrow H^- + h\nu, \tag{35}$$

$$H^- + H \rightarrow H_2 + e^-, \tag{36}$$

$$D^+ + H_2 \rightarrow HD + H^+. \tag{37}$$
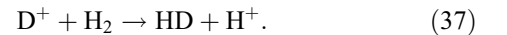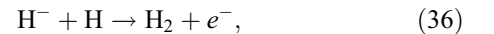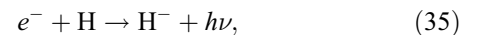
Since H$^-$ ions react as a catalyst to make hydrogen molecules, both H$_2$ and HD abundances increase while H$^-$ abundance increases, as in Figure 6 (*left*). The HD abundance continues to increase even after the H$^-$ abundance decreases and the H$_2$ abundance saturates. This is due to the charge transfer reaction in equation (37), through which HD molecules are formed from much more abundant H$_2$ molecules.

Figure 7 (*left*) plots the contributions from the cooling rates $\Lambda(T, n, \text{composition})$ for the same model as in Figure 6. This elucidates the fact that H$_2$ and HD molecules are effective coolants below the temperatures $\sim 2 \times 10^3$ and ~ 150 K, respectively. The cooling rate is smaller by a factor of 10^3 and 10^6 than the atomic cooling rate at its peak. If it were not for H$_2$ and HD molecules, however, gas could not be cooled below $\lesssim 10^4$ K within the Hubble time. In the model presented in Figure 7, the fractions of H$_2$ and HD molecules amount to $n(H_2)/n_{0,H} = 1.58 \times 10^{-3}$ and $n(HD)/n_{0,H} = 8.32 \times 10^{-6}$ at the fragmentation epoch, which are much larger than their primordial values of 10^{-6} and 10^{-9}, respectively (Galli & Palla 1998). These abundances agree well
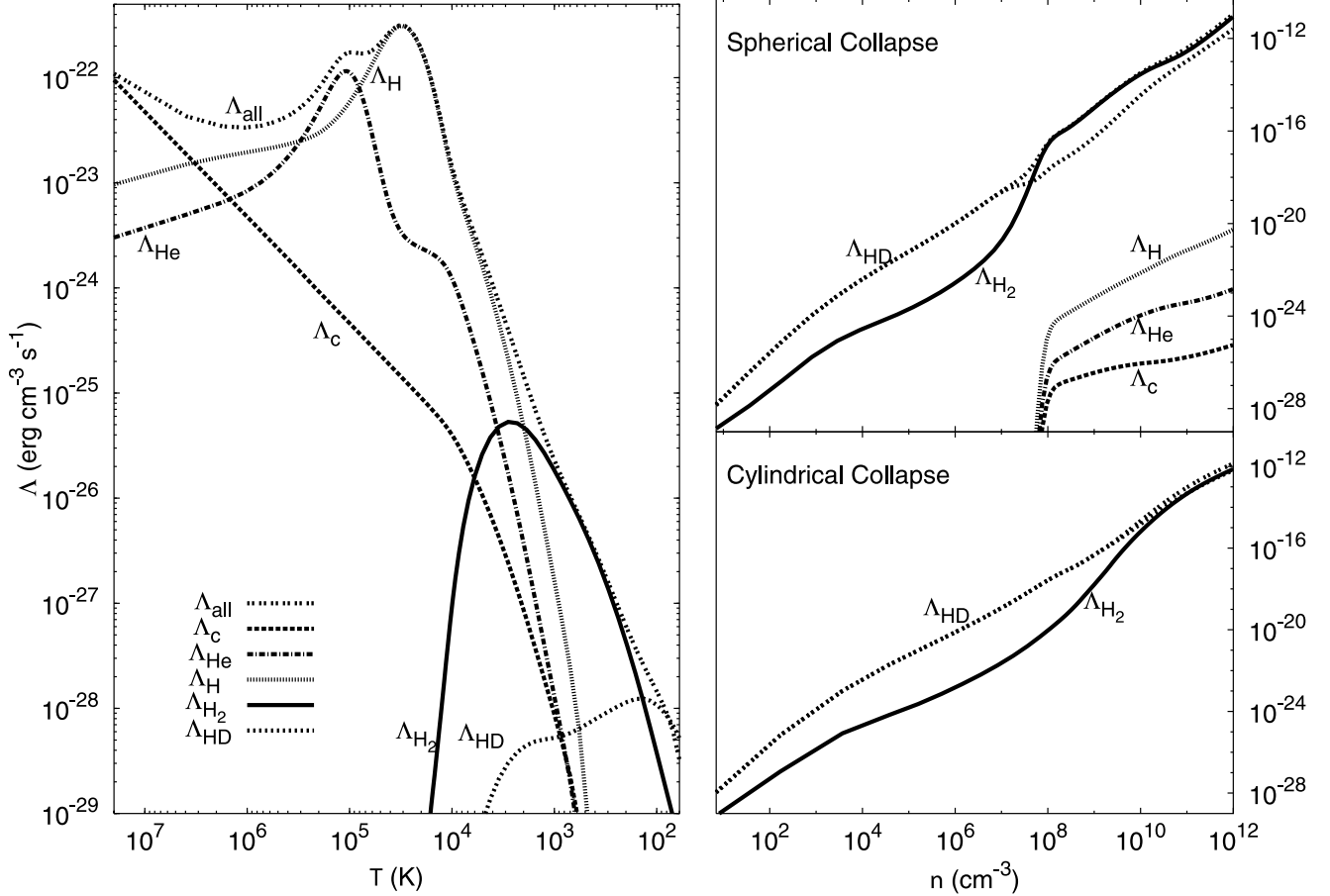
Fig. 7.—Cooling rates accomplished in the gas shell (Λ_{all}: total cooling rate, Λ_c: inverse Compton cooling, Λ_H: hydrogen cooling, Λ_{He}: helium cooling, Λ_{H_2}: molecular hydrogen cooling, and Λ_{HD}: HD molecular cooling) vs. gas temperature in the antefragmentation phase (*left*) and vs. number density in the post-fragmentation phase (*right*). Cooling rates in the case of spherical collapse (*top right*) and cylindrical collapse (*bottom right*) are shown. This corresponds to the model with $(z, \varepsilon_0) = (20,\ 10^{51}$ ergs). [*See the electronic edition of the Journal for a color version of this figure.*]

with the result of Uehara & Inutsuka (2000). When the temperature becomes as low as 145 K, the HD cooling exceeds the H$_2$ cooling and promotes a further drop in gas temperature. The fragmentation condition, $t_{\mathrm{ff}} = t_{\mathrm{dyn}}$, is satisfied only when the temperature descends to $T = 53$ K at the age of 14.7 Myr after the SN explosion. By this stage, the shell expands to a radius of 90 pc and the gas shell has gathered the ambient gas of mass 1.11×10^5 $M_\odot$ for this particular model.

3.2. *The Postfragmentation Phase*

After the condition of $\tau_{\mathrm{ff}} = \tau_{\mathrm{dyn}}$ is fulfilled, we assume fragmentation to occur. Then the evolution proceeds to the final stage of fragmentation and star formation. We follow the gravitational contraction of the fragment pieces assuming two different types of fragment geometry: sphere and cylinder.

The temperature evolution during the postfragmentation phase of the $(z, \varepsilon_0) = (20,\ 10^{51}$ ergs) model is shown in Figure 8 for both the spherical and cylindrical collapses. For the cylindrical case, the gas temperature T_c decreases to just above the CMB temperature. Fragmentation occurs at the age of 14.7 Myr after the SN explosion. At this epoch, $T_c \simeq 53$ K and $n_c \simeq 7$ cm^{-3}, which corresponds to a steep break near the lower left corner in Figure 8. Before the fragmentation, the evolutionary path in Figure 8 is vertically downward; that is, gas cools without strong compression. After this epoch, the fragment changes its evolution as it evolves nearly isothermally. The temperature of the fragment decreases further to 48 K, which decreases the critical

line mass $\lambda_c \propto T_c$ by 19% in 6.7 Myr from the fragmentation epoch. The shell expands from $R \simeq 90$ pc at $t = 14.7$ Myr to $R \simeq 103$ pc at $t = 28.7$ Myr, which increases the line mass λ by approximately 50%. These two factors work cooperatively to promote further collapse of the fragment. Thereafter, the fragment evolves under the condition that $\lambda_c \simeq \lambda$.

The gas temperature remains nearly constant for the number density $n \lesssim 10^6$ cm^{-3} and then increases to $T_c \sim 100$ K owing to the increase in the mean molecular weight, as also seen from Uehara & Inutsuka (2000). Variations in the fractional
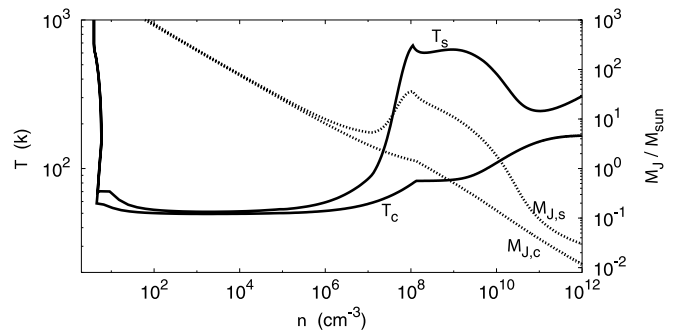

Fig. 8.—Evolution of gas temperature (T; *solid curves*) and Jeans mass (M_J; *dotted curves*) in the fragments during the postfragmentation phase for a model with $(z, \varepsilon_0) = (20,\ 10^{51}$ ergs). Two geometrical models of collapse are shown for spherical (T_s, $M_{J,s}$) and cylindrical (T_c, $M_{J,c}$) collapses. [*See the electronic edition of the Journal for a color version of this figure.*]

abundances are shown in Figure 6 (*right*) against the number density in the fragment pieces for the cylindrical contraction case. As the fragment contracts, the HD fraction gradually increases with density through the reaction in equation (37). The H_2 fraction changes little until the density becomes sufficiently high for the three-body reactions ($n \gtrsim 10^8$ cm^{-3}). A break near $n \simeq 10^8$ cm^{-3} in Figure 8 corresponds to this critical density of H_2. Beyond that density, the H_2 fraction starts to increase rapidly with density. The variations in the cooling rates are also plotted in the right panels of Figure 7 against the number density for both the spherical and cylindrical cases. H_2 and HD molecules are only the coolants effective after the fragmentation. It is clearly shown that HD molecules play a more important role in the lower temperature. HD molecules continue to dominate the cooling throughout the postfragmentation phase, which allows the contraction of the fragments at much lower temperatures than found in the previous computations involving only H_2 molecules (Puy et al. 1993; Uehara et al. 1996; Nakamura & Umemura 1999; Flower & Pineau des Forêts 2003).

For the spherical case, on the other hand, the temperature keeps rising with density owing to dynamical compression (Fig. 8). When the temperature becomes higher than $T_s \simeq 150$ K, HD molecules are dissociated to decrease the fractional abundance by a factor of $\sim 1/10$, and hence, the cooling rate due to HD molecules is overtaken by that due to H_2 molecules for $n \geq 10^8$ cm^{-3}. Thereafter, the H_2 fraction increases through the three-body reactions, which enhances the contribution of H_2 molecules to the cooling. Although the HD fraction also increases again through the charge exchange reaction with the H_2 molecules, the latter continues to dominate the cooling because of high temperatures. The temperature in the fragment pieces is, however, kept much lower than obtained in the previous computations without the HD molecules because of the lower temperatures at the fragmentation epoch (Ferrara 1998).

We also show the time variations in the Jeans masses in fragment pieces during the postfragmentation phase in Figure 8. For the cylindrical case, the Jeans mass $M_{J,c}$ decreases to 0.16 $M_\odot$ at the stage when fragment pieces become optically thick at the density $n \simeq 10^{10}$ cm^{-3}. After this stage, the cooling becomes ineffective and the gas cannot contract in the mass scale smaller than the Jeans mass, while the gas element more massive than the Jeans mass may collapse in a free-fall timescale. Because an adiabatic core is formed, further fragmentation can give rise to stars with the Jeans mass at the core formation epoch that is well below 1 $M_\odot$ and corresponds to a less massive star, which can survive to date. We note that our Jeans mass is larger than that of Uehara & Inutsuka (2000), $M_{J,c} \sim 0.04$ $M_\odot$, because they seem to underestimate the optical depths of HD lines (see e.g., Nakamura & Umemura 2002a). Therefore, our fragments are likely to evolve into low-mass stars rather than primordial brown dwarfs. For the spherical case, on the other hand, the fragment may not stop contracting even after it becomes optically thick (e.g., Omukai & Nishi 1998). However, since the gas shell is thin (the ratio of the thickness to the radius $\simeq 0.1$), the fragment pieces are expected to form a cylindrical filament whose axis is parallel to the shell and hence can give rise to stars with subsolar masses.

4. FRAGMENTATION CONDITIONS IN THE PRIMORDIAL CLOUDS

In the preceding section, we have solved the evolution of gas shells swept up by the SNRs of first-generation stars, assuming that the host clouds have sufficiently large masses. In order for star formation to be actually triggered in host clouds, the fol-

lowing two conditions have to be satisfied at the fragmentation epoch: (1) the shell expansion velocity is larger than the sound speed of ambient gas and (2) the mass of swept up gas is smaller than the total baryon mass of the host cloud. In our calculations, we have shown that the SNRs can give rise to low-mass star formation while the expansion velocity is larger than the ambient sound speed and hence avoid dissolving into the interstellar gas, except for the two cases of weakest explosion energy of $\varepsilon_0 = 1$ and 3×10^{51} ergs at the lowest collapse redshift of $z = 10$ (see V and $c_{s,hc}$ in Table 1, cols. [7] and [12]). Then the fragmentation occurs in the host cloud if the baryon mass of the host cloud is larger than the mass, M_{sw}, of the gas swept up by an SNR at the fragmentation epoch. If the expansion velocity is slowed to the ambient sound speed, the gas shell dissolves into the ambient gas. If a sufficient mass of gas is not available, SNRs expand beyond the edges of host clouds, either falling back and being mixed into the interstellar clouds or being dispersed out of clouds and spread into the intercloud space, depending on whether the expansion velocity is lower or greater than the escape velocity of the host clouds. We discuss below first the dependence on the mass of host clouds and then the effect of the ambient temperature.

The values of swept up gas mass, M_{sw}, at the fragmentation epoch are given in Table 1, which gives the minimum baryon masses of the host cloud necessary for the fragmentation under a given set of the ambient gas density (or collapse redshift) and the explosion energy. This mass varies by a factor of ~ 10 in the parameter range we computed from 6.07×10^4 to 8.04×10^5 $M_\odot$ and increases with the explosion energy and decreases for higher ambient gas density (or larger redshift at the collapse of the host cloud). This means that less massive host clouds can form low-mass stars only when they are formed in the earlier epoch (higher z and thus larger ρ_0).

The necessary baryon mass, M_{sw}, of the host cloud for the fragmentation can be converted into the total (baryon plus dark matter) mass of the host clouds by assuming an appropriate model of the universe. In Figure 9, we illustrate the permitted region (i.e., the baryon mass $\geq M_{sw}$) in the ε_0-z plane for various total masses by assuming the Einstein–de Sitter model, i.e., $\Omega_0 = 1$, $\Omega_B = 0.06$, and $M_T = M_{sw}(\Omega_0/\Omega_b)$. For a given mass of the host cloud, there exists a lower limit to the ambient gas density or the redshift of the supernova explosion that allows fragmentation of the gas shell; the lower limit is an increase function of ε_0. In the case of the first collapsed objects with total masses of $\sim 3 \times 10^6$ $M_\odot$ (see the shaded region of Fig. 9), fragmentation can occur within the host cloud in the shaded area of narrow parameters, e.g., if the supernova of $\varepsilon_0 = 3 \times 10^{51}$ ergs exploded at $z \gtrsim 20$ or that of $\varepsilon_0 = 10^{52}$ ergs exploded at $z \gtrsim 30$. Because of the rather narrow range of M_{sw} mentioned above, the mass of primordial clouds that can sustain supernova-triggered star formation is bounded sharply in the total cloud mass range $M_T \simeq 10^6$–10^7 $M_\odot$; that is, for the host clouds of $M_T = 2 \times 10^6$ $M_\odot$, supernova-triggered star formation is possible only in a narrow parameter region of $z \geq 20$ and $\varepsilon_0 < 3 \times 10^{51}$ ergs. For the host clouds of $M_T > 10^7$ $M_\odot$, star formation can always be triggered, except for the narrow range in the right bottom corner of $z \simeq 10$ and $\varepsilon_0 \simeq 10^{52}$ ergs.

We have also solved the thermal evolution of ambient gas consistently with the effect of the first-generation stars taken into account, to show that the temperature in the ambient gas decreases efficiently to the range of $T_{hc} = 193$–656 K by the time the fragment condition is satisfied (Table 1). By use of these temperatures, we can derive the condition that $V > c_{s,hc}(T_{hc})$, which is plotted by a thick line in the bottom left corner of
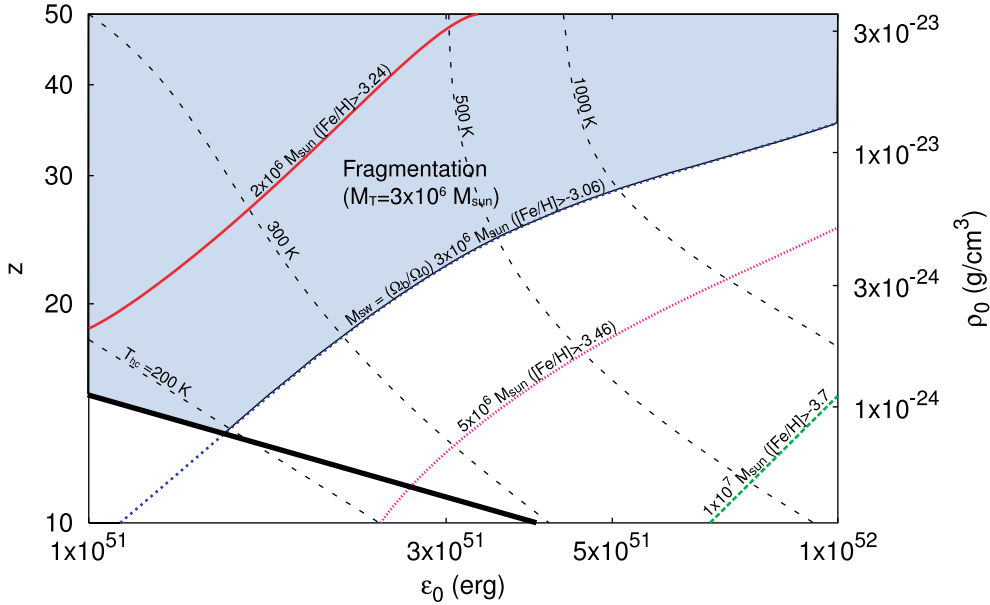
FIG. 9.—Lower bounds of the redshift z (*left axis*) or of the background density, ρ_0, in the host clouds (*right axis*) for star formation to be triggered by a single supernova explosion plotted as a function of the explosion energy, ε_0, of a supernova for host clouds of varying total mass, given mass $M_T = 2, 3, 5$, and $10 \times 10^6\ M_\odot$ (*from top to bottom*). The thick line denotes the border of $V = c_{s,\mathrm{hc}}(T)$, which divides whether the gas shell swept up by the SNR can fragment or merge into the ambient gas, with the temperature in the ambient gas derived by solving the chemical reaction and thermal evolution of the ambient gas simultaneously. For example, the shaded region denotes the parameter range in which we expect the SNR-induced fragmentation of low-mass second-generation stars in the host clouds with a total mass of $M_T = 3 \times 10^6\ M_\odot$. Dotted lines represent the dependence on the shell expansion speed (or the temperature) in the ambient gas for temperatures of 200, 300, 500, and 1000 K. They give the boundaries for the gas shell, swept up by the SNR, to fragment without mixing into the ambient matter; i.e., supernova-triggered, low-mass star formation is expected in the parameter range to the right of these lines and requires a supernova of larger explosion energy for higher temperatures in the ambient gas. For the supernova of weaker energy, the SNR shell dissolves into the ambient gas before the fragmentation.

Figure 9. In the parameter region above and to the right of this line, i.e., if a supernova explodes with a larger explosion in the host cloud of higher density than delineated by this line, the gas shell swept up by the SNR can fragment to give birth to low-mass stars surviving to the present. Otherwise, the swept up gas shell will dissolve and merge into the ambient gas without triggering fragmentation.

In the above computations, we take into account the heating of ambient gas only by the SN progenitor, which ends with the supernova explosion. The temperatures in the ambient gas may vary and can be higher, however, if gas is irradiated by other heating sources, such as other first-generation massive stars or the SNR itself, and/or if the SNR shell expands beyond the Strömgren sphere, in which the temperature has not been raised high enough to ionize gas and hence the subsequent cooling is not so effective. In order to see the dependence of the evolution and fragmentation of the SNR gas shell on the thermal state of ambient gas, we calculate the evolution of several SNR models with the temperature of ambient gas set at a constant value, i.e., $T_{\mathrm{hc}} = T_0$. For $z = 20$ and $\varepsilon = 10^{51}$ ergs, the gas shell expands and cools enough to meet the fragment condition $\tau_{\mathrm{ff}} = \tau_{\mathrm{dyn}}$ when the SNR radius reaches 92 and 85 pc in the models of constant ambient temperature $T_{\mathrm{hc}} = 200$ and 10^3 K, respectively. The difference in the radii reflects the effect of deceleration by the ambient gas pressure. The condition under which the swept up gas shell keeps expanding without being dissolved into the ambient medium ($V > c_{s,\mathrm{hc}}$) is satisfied in the model of the lower ambient temperature, consistent with the above result of the calculation that solves the thermal evolution of ambient gas simultaneously. In the model of $T_{\mathrm{hc}} = 10^3$ K, this condition is violated earlier; hence, the gas shell has to be disturbed and merges into the ambient medium before it can gather gas sufficient to trigger the fragmentation. For such a high ambient temperature as $T_{\mathrm{hc}} = 10^4$ K, the expansion of the SNR is halted

at the radius of 52 pc because of the high pressure of the ambient medium, and the swept up gas shell will be dissolved and melted in the host cloud.

In Figure 9, we also show the parameter region, where the conditions of $V = c_{s,\mathrm{hc}}(T_{\mathrm{hc}})$ are satisfied until the fragmentation epoch, using dotted lines for the different ambient temperatures of $T_{\mathrm{hc}} = 200, 300, 500$, and 10^3 K. In the parameter range left of these lines, where $V < c_s(T_{\mathrm{hc}})$, the SNR shell is dissolved into the ambient medium before the fragmentation epoch for a given ambient temperature $T_{\mathrm{hc}} = T_0$. If the ambient temperature is kept higher, the fragmentation demands a supernova of greater explosion energy, since the SNR has to sweep up the amount of ambient gas necessary for fragmentation before the expansion is decelerated to sound velocity in the ambient gas. For example, if the ambient medium has been cooled to 300 K by radiative cooling, the explosion energy of $\varepsilon_0 \gtrsim 2 \times 10^{51}$ ergs is necessary for $V > c_{s,\mathrm{hc}}(300\ \mathrm{K})$ in a host cloud of $M_T = 3 \times 10^6\ M_\odot$ at $z = 20$, while for the cloud with $T_{\mathrm{hc}} = 1000$ K, a much stronger explosion energy of $\varepsilon_0 \gtrsim 5 \times 10^{51}$ ergs is necessary for the SNR shell to fragment. For a high temperature of $T_{\mathrm{hc}} \sim 10^4$ K, such as assumed by Salvaterra et al. (2004), SN-triggered star formation is possible only for a supernova (or hypernova) with an explosion energy exceeding 10^{52} ergs, consistent with their results. However, this is not the case, since it is likely that gas in the host cloud has been cooled after the supply of UV photons from the SN progenitor ceased.

5. CONCLUSIONS AND DISCUSSION

In this paper, we have addressed two questions: whether a primordial SNR can trigger star formation in a first collapsed object and whether low-mass stars can be formed that could survive to the present. For that purpose, we have studied the evolution of supernova remnants in primordial clouds with H_2 and HD chemistry taken into account for a range of parameters

of ambient density (or redshift) of host clouds and explosion energy of supernovae, as summarized in Table 1. It is found that a gas shell swept up by a supernova shock undergoes cooling and that HD molecules can effectively cool the temperature to as low as 32–154 K. Fragmentation begins when the mass in the gas shell reaches the range of 6.1×10^4 to 8.0×10^5 $M_\odot$. This is the necessary mass, M_{sw}, for star formation to be triggered by SNRs in primordial clouds of total mass M_T; M_{sw} depends on the ambient density (or the redshift) and the SN explosion energy. The standard cold dark matter model predicts that the masses of the collapsed objects from the 3 σ peaks vary from $M_T \simeq 2 \times 10^6$ $M_\odot$ at $z = 30$ to $\simeq 10^8$ $M_\odot$ at $z = 10$ (e.g., Haiman et al. 1996; Tegmark et al. 1997), with corresponding baryon masses of $M_b \simeq 10^5$ $M_\odot$ ($z = 30$) and $M_b \simeq 5 \times 10^6$ $M_\odot$ ($z = 10$). If $M_{sw} < M_b = \Omega_B M_T$, the SNR can fragment within the host cloud to bring about supernova-triggered star formation. Otherwise, the gas shell passes the edge of the host cloud and hence is blown out without fragmentation.

In the range of parameters studied, fragmentation occurs in the pressure-driven expansion stage. The SNR expands to radii of 30–332 pc by this stage, which increases with the explosion energy and decreases with the ambient density. It takes 1.1–45 Myr from the supernova explosion, much shorter than the Hubble age at that epoch, for the swept up gas shell to start fragmentation, which is shorter for higher ambient density and for larger supernova explosion energy. The lifetimes of massive stars (several tens of solar masses) as $\tau \simeq 10$ Myr are longer than the elapsed time for high-z SNRs ($t_f \lesssim 5$ Myr for $z = 50$ models) and at least comparable for the supernova explosion at lower redshift ($t_f \simeq 10$ Myr for $z = 20$ models). Accordingly, it may be possible that fragmentation occurs even before other subsequent supernovae in the same primordial clouds contaminate the swept up gas shell.

5.1. Fate of Stars Formed by This Mechanism

We discuss the fate of host clouds after the low-mass stars have formed in the gas shell. We evaluate the systematic expansion velocity V expected for newborn stars from the expanding velocity of a gas shell at fragmentation in Table 1. The escape velocities, V_{esc}, of the host clouds are also summarized in Table 1 and are evaluated from the total (baryon + dark matter) mass contained in the SNR shell radius at the fragmentation epoch, $M_T = M_{sw}(\Omega_0/\Omega_b)$, as

$$V_{esc} \simeq \left(\frac{2GM_T}{R}\right)^{1/2} = \left(\frac{2GM_{sw}}{R}\right)^{1/2} \left(\frac{\Omega_0}{\Omega_b}\right)^{1/2}, \quad (38)$$

where M_{sw} represents the contained baryon mass. If $V < V_{esc}$, the second-generation low-mass stars remain within the host cloud. Since the mass of the host cloud is larger than the minimum mass of fragmentation $M_{sw}(\Omega_0/\Omega_b)$, all the models calculated predict that newborn stars are bounded.

Otherwise, the newborn stars will escape from the host cloud and be ejected into intergalactic space. This does not occur in our models. This tendency is consistent with the SPH simulation of SNRs formed in low-mass minihalos $M \sim 10^6$ $M_\odot$ by Bromm et al. (2003). That is, in a low-energy model with $\varepsilon_0 = 10^{51}$ ergs the halo (cloud) is unchanged, while an SN with $\varepsilon_0 = 10^{53}$ ergs disrupts the halo (cloud).

In our calculations, the fragments are likely to be bounded in the host cloud because the velocity of the fragments is lower than the escape velocity estimated by the swept up mass for all the models we studied. We only investigate the explosion energy of 10^{51}–10^{52} ergs. If more energetic supernovae, such as pair-
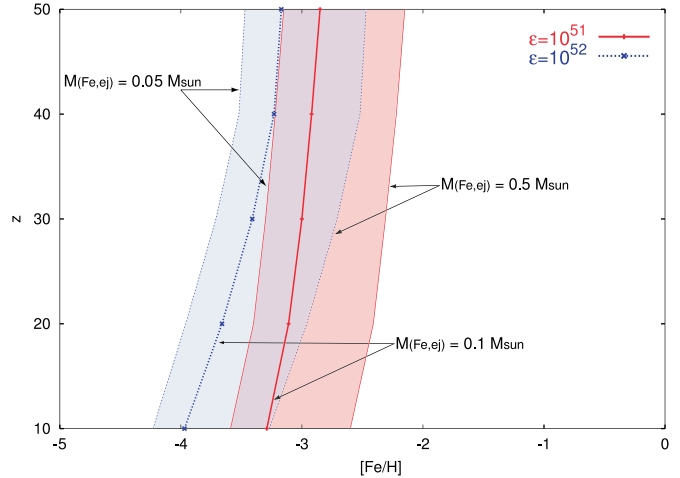

Fig. 10.—Expected metallicity of [Fe/H] vs. initial z. [Fe/H] is estimated by the ratio of the swept up mass and the ejected iron mass. Ejected iron mass is assumed to be $M_{Fe,ej} = 0.1$ $M_\odot$ (thick center lines), 0.05 $M_\odot$ (left border lines), and 0.5 $M_\odot$ (right border lines), estimated by Tsujimoto & Shigeyama (1998). Models $\varepsilon_0 = 10^{51}$ ergs (solid lines) and $\varepsilon_0 = 10^{52}$ ergs (dotted lines).

instability supernovae with $\varepsilon_0 > 10^{52}$ ergs, occur, newborn stars escape from the host cloud because their velocities are higher than the escape velocity. When the SNR escapes from the host cloud without fragmentation, the gas, which has large H_2 and HD abundances, drifts in the intergalactic medium.

5.2. Metal Abundance

In the preceding section, we have assumed the primordial abundances of elements for the gas shell. The fragments, and in particular the stars formed out of them, are expected to be polluted by metals ejected from the SN, although the degree of metal abundance may vary with the efficiency of mixing between the SN ejecta and the surrounding material. Assuming complete mixing, we can evaluate the metal abundance in the gas shell. If the ejected mass of iron, $M_{ej,Fe}$ (Tsujimoto & Shigeyama 1998), is mixed with the swept up mass, M_{sw}, this gives

$$[\text{Fe/H}] \simeq -2.8 + \log_{10}\left[\frac{M_{ej,Fe}}{0.1\ M_\odot}\left(\frac{M_{sw}}{5 \times 10^4\ M_\odot}\right)^{-1}\right], \quad (39)$$

where the solar abundance of iron is assumed to be equal to 1.16×10^{-3}. Figure 10 shows the expected value of [Fe/H]. From this figure, we found that the next-generation stars triggered by primordial SNRs have a metallicity of [Fe/H] $\simeq -2.5$ to -4.5. The upper limit corresponds to a low explosion energy $\varepsilon_0 = 10^{51}$ ergs and a high-mass iron ejection $M_{ej,Fe} = 0.5$ $M_\odot$, while the other limit corresponds to the high explosion energy $\varepsilon_0 = 10^{52}$ ergs and a low-mass iron ejection $M_{ej,Fe} = 0.05$ $M_\odot$. The actual distributions of metallicity realized in the SNR, however, have to have a scatter around this mean value. It should be pointed out that the metal abundance of the low-mass stars formed by the supernova resembles that of the extremely metal-deficient stars in the Galactic halo ([Fe/H] ~ -3) discovered by the large-scale survey by Beers et al. (1992). However, the most metal-deficient ([Fe/H] $= -5.3$) star that has been found, HE 0107$-$5240 (Christlieb et al. 2002), has too little metallicity to be explained by the mixture of SN ejecta of a first-generation massive star and the primordial gas swept up in its SNR shell. This seems to mean that HE 0107$-$5240 was not formed in a cloud with M_T around several $\times 10^6$ $M_\odot$.

How does the ejecta gas mix with a 100 times more massive cloud composed of primordial gas? Consider a cloud with smaller mass as $M_T \sim 10^6 \, M_\odot$. The SNR shell sweeps up all the gas in such a cloud, and the swept up shell, as well as the gas ejected from the SN, is ejected into the intracloud space. In this case, metals mix not with the cloud medium but with the intracloud medium. If this cloud belongs to a more massive density perturbation with $M_T \sim 10^8 \, M_\odot$, such a system contracts later and forms stars with 100 times more deficient metallicity than the above-mentioned star formed in the cloud M_T around several $\times 10^6 \, M_\odot$.

Specifically, our results suggest that the characteristic element abundances of ejecta from a single Population III supernova can be imprinted on the abundance distributions in these extremely metal-poor stars. Their relevance is worthy of further study, and if their connection is confirmed, we may gain information on the first collapsed objects in our universe from the current status of these survivors.

APPENDIX A

RADIATIVE COOLING PROCESS

As the radiative cooling process, we include the inverse Compton process owing to the cosmic background radiation, and line cooling of H, He, H_2, and HD. In this Appendix we briefly summarize the cooling rate. The units of the cooling rate are ergs $cm^{-3} \, s^{-1}$, and that of the temperature is kelvins.

1. Inverse Compton cooling (Ikeuchi & Ostriker 1986):

$$\Lambda_{ic} = 5.41 \times 10^{-32}(1+z)^4 \left(\frac{T}{10^4}\right) n_e. \tag{A1}$$

2. Helium cooling
   (a) Collisional ionization cooling (Cen 1992):

$$\Lambda_{He,cl} = 9.38 \times 10^{-22} T^{1/2} \left[1 + \left(\frac{T}{10^5}\right)^{1/2}\right]^{-1} \exp\frac{-285335.4}{T} n_e n_{He}, \tag{A2}$$

$$\Lambda_{He^+,cl} = 4.95 \times 10^{-22} T^{1/2} \left[1 + \left(\frac{T}{10^5}\right)^{1/2}\right]^{-1} \exp\frac{-631515}{T} n_e n_{He^+}, \tag{A3}$$

$$\Lambda'_{He^+,cl} = 5.01 \times 10^{-27} T^{-0.1687} \left[1 + \left(\frac{T}{10^5}\right)^{1/2}\right]^{-1} \exp\frac{-55338}{T} n_e^2 n_{He^+}. \tag{A4}$$

   (b) Recombination cooling (Cen 1992):

$$\Lambda_{He^+,re} = 1.55 \times 10^{-26} T^{0.3647} n_e n_{He^+}, \tag{A5}$$

$$\Lambda_{He^{++},re} = 3.48 \times 10^{-26} T^{1/2} \left(\frac{T}{10^3}\right)^{-0.2} \left[1 + \left(\frac{T}{10^6}\right)^{0.7}\right]^{-1} n_e n_{He^{++}}. \tag{A6}$$

   (c) Collisional excitation cooling (Cen 1992):

$$\Lambda_{He^+,ex} = 5.54 \times 10^{-17} T^{-0.397} \left[1 + \left(\frac{T}{10^5}\right)^{1/2}\right]^{-1} \exp\frac{-473638}{T} n_e n_{He^+}, \tag{A7}$$

$$\Lambda_{He^{++},ex} = 9.10 \times 10^{-27} T^{-0.1687} \left[1 + \left(\frac{T}{10^5}\right)^{1/2}\right]^{-1} \exp\frac{-13179}{T} n_e^2 n_{He^+}. \tag{A8}$$

3. Hydrogen cooling
   (a) Collisional ionization cooling (Cen 1992):

$$\Lambda_{H,cl} = 1.27 \times 10^{-21} T^{1/2} \left[1 + \left(\frac{T}{10^5}\right)^{1/2}\right]^{-1} \exp\frac{-157809.1}{T} n_e n_H. \tag{A9}$$

(*b*) Recombination cooling (Cen 1992):

$$\Lambda_{\mathrm{H,re}} = 8.70 \times 10^{-27} T^{1/2} \left(\frac{T}{10^3}\right)^{-0.2} \left[1 + \left(\frac{T}{10^6}\right)^{0.7}\right]^{-1} n_e n_{\mathrm{H^+}}. \tag{A10}$$

(*c*) Collisional excitation cooling (Cen 1992):

$$\Lambda_{\mathrm{H,ex}} = 7.5 \times 10^{-19} \left[1 + \left(\frac{T}{10^5}\right)^{1/2}\right]^{-1} \exp\frac{-118348}{T} n_e n_{\mathrm{H}}. \tag{A11}$$

4. Molecule hydrogen cooling: $\Lambda_{\mathrm{H_2}}$ is taken from the table of Flower et al. (2000).
5. HD cooling: Λ_{HD} is taken from the table of Flower et al. (2000).
6. Effect of the CMB radiation:

$$\Lambda_{\mathrm{CMB}} = \Lambda_{\mathrm{H_2}}(T_{\mathrm{CMB}}) + \Lambda_{\mathrm{HD}}(T_{\mathrm{CMB}}), \tag{A12}$$

where T_{CMB} is taken as $2.73(1+z)$.

APPENDIX B

CHEMICAL REACTIONS

We include the chemical reactions of 12 species: H, H$^+$, H$^-$, He, He$^+$, He^{++}, H$_2$, D, D$^+$, HD, HD$^+$, and e^-. In this Appendix we summarize the reactions we adopt.

$$\begin{aligned}
\frac{dn_{\mathrm{H}}}{dt} = {} & k_2 n_{\mathrm{H^+}} n_e + 2k_{12} n_{\mathrm{H_2}} n_e + k_{13} n_{\mathrm{H^-}} n_e + 2k_{14} n_{\mathrm{H^-}} n_{\mathrm{H^+}} + k_{20} n_{\mathrm{D}} n_{\mathrm{H^+}} k_{22} n_{\mathrm{D}} n_{\mathrm{H_2}} + k_9 n_{\mathrm{H}} n_{\mathrm{H}} n_{\mathrm{H}} + 3k_{10} n_{\mathrm{H2}} n_{\mathrm{H}} \\
& + k_{11} n_{\mathrm{H_2}} n_{\mathrm{H^+}} + 2k_{16} n_{\mathrm{H_2}} n_{\mathrm{H_2}} + k_{17} n_{\mathrm{H}} n_{\mathrm{H}} - k_1 n_{\mathrm{H}} n_e - k_7 n_{\mathrm{H}} n_e - k_8 n_{\mathrm{H}} n_{\mathrm{H^-}} - k_{21} n_{\mathrm{D^+}} n_{\mathrm{H}} \\
& - k_{24} n_{\mathrm{HD^+}} n_{\mathrm{H}} - k_{28} n_{\mathrm{D^+}} n_{\mathrm{H}} - 3k_9 n_{\mathrm{H}} n_{\mathrm{H}} n_{\mathrm{H}} - k_{10} n_{\mathrm{H_2}} n_{\mathrm{H}} - 2k_{15} n_{\mathrm{H}} n_{\mathrm{H}} n_{\mathrm{H_2}} - 2k_{17} n_{\mathrm{H}} n_{\mathrm{H}},
\end{aligned} \tag{B1}$$

$$\begin{aligned}
\frac{dn_{\mathrm{H^+}}}{dt} = {} & k_1 n_{\mathrm{H}} n_e + k_{21} n_{\mathrm{D^+}} n_{\mathrm{H}} + k_{23} n_{\mathrm{HD^+}} n_{\mathrm{H^+}} + k_{24} n_{\mathrm{D^+}} n_{\mathrm{H_2}} + k_{17} n_{\mathrm{H}} n_{\mathrm{H}} - k_2 n_{\mathrm{H^+}} n_e \\
& - k_{11} n_{\mathrm{H_2}} n_{\mathrm{H^+}} - k_{14} n_{\mathrm{H^-}} n_{\mathrm{H^+}} - k_{20} n_{\mathrm{D}} n_{\mathrm{H^+}} - k_{26} n_{\mathrm{HD}} n_{\mathrm{H^+}} - k_{27} n_{\mathrm{D}} n_{\mathrm{H^+}},
\end{aligned} \tag{B2}$$

$$\frac{dn_{\mathrm{H^-}}}{dt} = k_7 n_{\mathrm{H}} n_e - k_8 n_{\mathrm{H}} n_{\mathrm{H^-}} - k_{13} n_{\mathrm{H^-}} n_e - k_{14} n_{\mathrm{H^-}} n_{\mathrm{H^+}}, \tag{B3}$$

$$\frac{dn_{\mathrm{He}}}{dt} = k_4 n_{\mathrm{He^+}} n_e - k_3 n_{\mathrm{He}} n_e, \tag{B4}$$

$$\frac{dn_{\mathrm{He^+}}}{dt} = k_3 n_{\mathrm{He}} n_e + k_6 n_{\mathrm{He^{++}}} n_e - k_4 n_{\mathrm{He^+}} n_e - k_5 n_{\mathrm{He^+}} n_e, \tag{B5}$$

$$\frac{dn_{\mathrm{He^{++}}}}{dt} = k_5 n_{\mathrm{He^+}} n_e - k_6 n_{\mathrm{He^{++}}} n_e, \tag{B6}$$

$$\begin{aligned}
\frac{dn_{\mathrm{H_2}}}{dt} = {} & k_8 n_{\mathrm{H}} n_{\mathrm{H^-}} + k_{26} n_{\mathrm{HD}} n_{\mathrm{H^+}} + k_9 n_{\mathrm{H}} n_{\mathrm{H}} n_{\mathrm{H}} + 2k_{15} n_{\mathrm{H}} n_{\mathrm{H}} n_{\mathrm{H_2}} + k_{16} n_{\mathrm{H_2}} n_{\mathrm{H_2}} - k_{11} n_{\mathrm{H_2}} n_{\mathrm{H^+}} \\
& - k_{12} n_{\mathrm{H_2}} n_e - k_{22} n_{\mathrm{D}} n_{\mathrm{H_2}} - k_{24} n_{\mathrm{D^+}} n_{\mathrm{H_2}} - k_{10} n_{\mathrm{H_2}} n_{\mathrm{H}} - k_{15} n_{\mathrm{H}} n_{\mathrm{H}} n_{\mathrm{H_2}} - 2k_{16} n_{\mathrm{H_2}} n_{\mathrm{H_2}},
\end{aligned} \tag{B7}$$

$$\frac{dn_{\mathrm{D}}}{dt} = k_{18} n_{\mathrm{D^+}} n_e + k_{21} n_{\mathrm{D^+}} n_{\mathrm{H}} + k_{25} n_{\mathrm{HD}} n_{\mathrm{H}} - k_{19} n_{\mathrm{D}} n_e - k_{20} n_{\mathrm{D}} n_{\mathrm{H^+}} - k_{22} n_{\mathrm{D}} n_{\mathrm{H_2}}, \tag{B8}$$

$$\frac{dn_{\mathrm{D^+}}}{dt} = k_{20} n_{\mathrm{D}} n_{\mathrm{H^+}} + k_{26} n_{\mathrm{HD}} n_{\mathrm{H^+}} - k_{18} n_{\mathrm{D^+}} n_e - k_{21} n_{\mathrm{D^+}} n_{\mathrm{H}} - k_{24} n_{\mathrm{D^+}} n_{\mathrm{H_2}} - k_{28} n_{\mathrm{D^+}} n_{\mathrm{H}}, \tag{B9}$$

$$\frac{dn_{\mathrm{HD}}}{dt} = k_{22} n_{\mathrm{D}} n_{\mathrm{H_2}} + k_{23} n_{\mathrm{HD^+}} n_{\mathrm{H}} + k_{24} n_{\mathrm{D^+}} n_{\mathrm{H_2}} - k_{26} n_{\mathrm{HD}} n_{\mathrm{H^+}}, \tag{B10}$$

$$\frac{dn_{\mathrm{HD^+}}}{dt} = k_{27} n_{\mathrm{D}} n_{\mathrm{H^+}} + k_{28} n_{\mathrm{D^+}} n_{\mathrm{H}} - k_{23} n_{\mathrm{HD^+}} n_{\mathrm{H}}. \tag{B11}$$

The reaction rates for the above reactions are taken from Palla et al. (1983), Shapiro & Kang (1987), Abel et al. (1997), Galli & Palla (1998), and Stancil et al. (1998). See Table 2 for reaction rate coefficients.

TABLE 2
REACTION RATE COEFFICIENTS

Number	Reaction	Rate $(\mathrm{cm^{-3}\,s^{-1}})$	Reference
(1)	$\mathrm{H} + e \rightarrow \mathrm{H^+} + 2e$	$\begin{aligned} k_1 = \exp[&-32.71396786 \\ &+13.536556 \ln(T/\mathrm{eV}) \\ &-5.73932875 \ln(T/\mathrm{eV})^2 \\ &+1.56315498 \ln(T/\mathrm{eV})^3 \\ &-0.2877056 \ln(T/\mathrm{eV})^4 \\ &+3.48255977 \times 10^{-2} \ln(T/\mathrm{eV})^5 \\ &-2.63197617 \times 10^{-3} \ln(T/\mathrm{eV})^6 \\ &+1.11954395 \times 10^{-4} \ln(T/\mathrm{eV})^7 \\ &-2.03914985 \times 10^{-6} \ln(T/\mathrm{eV})^8] \end{aligned}$	1
(2)	$\mathrm{H^+} + e \rightarrow \mathrm{H} + \gamma$	$\begin{aligned} k_2 = \exp[&-28.6130338 \\ &-0.72411256 \ln(T/\mathrm{eV}) \\ &-2.02604473 \times 10^{-2} \ln(T/\mathrm{eV})^2 \\ &-2.38086188 \times 10^{-3} \ln(T/\mathrm{eV})^3 \\ &-3.21260521 \times 10^{-4} \ln(T/\mathrm{eV})^4 \\ &-1.42150291 \times 10^{-5} \ln(T/\mathrm{eV})^5 \\ &+4.98910892 \times 10^{-6} \ln(T/\mathrm{eV})^6 \\ &+5.75561414 \times 10^{-7} \ln(T/\mathrm{eV})^7 \\ &-1.85676704 \times 10^{-8} \ln(T/\mathrm{eV})^8 \\ &-3.07113524 \times 10^{-9} \ln(T/\mathrm{eV})^9] \end{aligned}$	1
(3)	$\mathrm{He} + e \rightarrow \mathrm{He^+} + 2e$	$\begin{aligned} k_3 = \exp[&-44.09864886 \\ &+23.91596563 \ln(T/\mathrm{eV}) \\ &-10.7532302 \ln(T/\mathrm{eV})^2 \\ &+3.05803875 \ln(T/\mathrm{eV})^3 \\ &-0.56851189 \ln(T/\mathrm{eV})^4 \\ &+6.79539123 \times 10^{-2} \ln(T/\mathrm{eV})^5 \\ &-5.00905610 \times 10^{-3} \ln(T/\mathrm{eV})^6 \\ &+2.06723616 \times 10^{-4} \ln(T/\mathrm{eV})^7 \\ &-3.694916141 \times 10^{-6} \ln(T/\mathrm{eV})^8] \end{aligned}$	1
(4)	$\mathrm{He^+} + e \rightarrow \mathrm{He} + \gamma$	$k_4 = 3.925 \times 10^{-13} (T/\mathrm{eV})^{-0.6353}$	1
(5)	$\mathrm{He^+} + e \rightarrow \mathrm{He^{++}} + 2e$	$\begin{aligned} k_5 = \exp[&-68.71040990 \\ &+43.93347633 \ln(T/\mathrm{eV}) \\ &-18.4806699 \ln(T/\mathrm{eV})^2 \\ &+4.70162649 \ln(T/\mathrm{eV})^3 \\ &-0.76924663 \ln(T/\mathrm{eV})^4 \\ &+8.113042 \times 10^{-2} \ln(T/\mathrm{eV})^5 \\ &-5.32402063 \times 10^{-3} \ln(T/\mathrm{eV})^6 \\ &+1.97570531 \times 10^{-4} \ln(T/\mathrm{eV})^7 \\ &-3.16558106 \times 10^{-6} \ln(T/\mathrm{eV})^8] \end{aligned}$	1
(6)	$\mathrm{He^{++}} + e \rightarrow \mathrm{He^+} + \gamma$	$k_6 = 3.3610^{-10} T^{-1/2} (T/1000)^{-0.2} [1 + (T/10^6)^{0.7}]^{-1}$	1
(7)	$\mathrm{H} + e \rightarrow \mathrm{H^-} + \gamma$	$k_7 = \begin{cases} 1.0 \times 10^{-18} T & T < 1.5 \times 10^4 \text{ K,} \\ \mathrm{dex}[-14.10 & \\ \quad +0.1175 \log T & \\ \quad -9.813 \times 10^{-3}(\log T)^2] & T > 1.5 \times 10^4 \text{ K} \end{cases}$	2
(8)	$\mathrm{H} + \mathrm{H^-} \rightarrow \mathrm{H_2} + e$	$k_8 = \begin{cases} \exp[-20.06913897 & \\ \quad +0.22898 \ln(T/\mathrm{eV}) & \\ \quad +3.5998377 \times 10^{-2} \ln(T/\mathrm{eV})^2 & \\ \quad -4.55512 \times 10^{-3} \ln(T/\mathrm{eV})^3 & \\ \quad -3.10511544 \times 10^{-4} \ln(T/\mathrm{eV})^4 & \\ \quad +1.0732940 \times 10^{-4} \ln(T/\mathrm{eV})^5 & \\ \quad -8.36671960 \times 10^{-6} \ln(T/\mathrm{eV})^6 & \\ \quad +2.23830623 \times 10^{-7} \ln(T/\mathrm{eV})^7] & T > 1160 \text{ K,} \\ 1.428 \times 10^{-9} & T < 1160 \text{ K} \end{cases}$	1
(9)	$\mathrm{H} + \mathrm{H} + \mathrm{H} \rightarrow \mathrm{H_2} + \mathrm{H}$	$k_9 = 5.5 \times 10^{-29} T^{-1}$	3
(10)	$\mathrm{H_2} + \mathrm{H} \rightarrow \mathrm{H} + \mathrm{H} + \mathrm{H}$	$k_{10} = 6.5 \times 10^{-7} T^{-1/2} \exp(-52000/T) \times [1 - \exp(-6000/T)]$	3
(11)	$\mathrm{H_2} + \mathrm{H^+} \rightarrow \mathrm{H_2^+} + \mathrm{H}$	$\begin{aligned} k_{11} = \exp[&-24.24914687 \\ &+3.4008244 \ln(T/\mathrm{eV}) \\ &-3.89800396 \ln(T/\mathrm{eV})^2 \\ &+2.04558782 \ln(T/\mathrm{eV})^3 \\ &-0.541618285 \ln(T/\mathrm{eV})^4 \\ &+8.41077503 \times 10^{-2} \ln(T/\mathrm{eV})^5 \\ &-7.87902615 \times 10^{-3} \ln(T/\mathrm{eV})^6 \\ &+4.13839842 \times 10^{-4} \ln(T/\mathrm{eV})^7 \\ &-9.3634588 \times 10^{-6} \ln(T/\mathrm{eV})^8] \end{aligned}$	1

TABLE 2—*Continued*

Number	Reaction	Rate (cm^{-3} s^{-1})	Reference
(12)	$H_2 + e \rightarrow 2H + e$	$k_{12} = 5.6 \times 10^{-11} T^{1/2} \exp(-102124/T)$	1
(13)	$H^- + e \rightarrow H + 2e$	$k_{13} = \exp[-18.01849334$ $+2.3608522 \ln(T/eV)$ $-0.28274430 \ln(T/eV)^2$ $+1.62331664 \times 10^{-2} \ln(T/eV)^3$ $-3.36501203 \times 10^{-2} \ln(T/eV)^4$ $+1.17832978 \times 10^{-2} \ln(T/eV)^5$ $-1.65619470 \times 10^{-3} \ln(T/eV)^6$ $+1.06827520 \times 10^{-4} \ln(T/eV)^7$ $-2.63128581 \times 10^{-6} \ln(T/eV)^8]$	1
(14)	$H^- + H^+ \rightarrow 2H$	$k_{14} = 7 \times 10^{-8} (T/100)^{-1/2}$	1
(15)	$H + H + H_2 \rightarrow H_2 + H_2$	$k_{15} = 6.875 \times 10^{-30} T^{-1}$	3
(16)	$H_2 + H_2 \rightarrow H + H + H_2$	$k_{16} = 8.0 \times 10^{-8} T^{-1/2} \exp(-52000/T)$ $\times [1 - \exp(-6000/T)]$	3
(17)	$H + H \rightarrow H^+ + e + H$	$k_{17} = 9.86 \times 10^{-15} T^{0.5} \exp(-158000/T)$	3
(18)	$D^+ + e \rightarrow D + \gamma$	$k_{18} = 3.6 \times 10^{-12} (T/300)$	4
(19)	$D + e \rightarrow D^- + \gamma$	$k_{19} = 3.0 \times 10^{-16} (T/300)^{0.95} \exp(-T/9320)$	4
(20)	$D + H^+ \rightarrow D^+ + H$	$k_{20} = 3.7 \times 10^{-10} T^{0.28} \exp(-43/T)$	4
(21)	$D^+ + H \rightarrow D + H^+$	$k_{21} = 3.7 \times 10^{-10} T^{0.28}$	4
(22)	$D + H_2 \rightarrow H + HD$	$k_{22} = 9 \times 10^{-11} \exp(-3876/T)$	4
(23)	$HD^+ + H \rightarrow H^+ + HD$	$k_{23} = 6.4 \times 10^{-10}$	4
(24)	$D^+ + H_2 \rightarrow H^+ + HD$	$k_{24} = 2.1 \times 10^{-9}$	4
(25)	$HD + H \rightarrow H_2 + D$	$k_{25} = 3.2 \times 10^{-11} \exp(-3624/T)$	4
(26)	$HD + H^+ \rightarrow H_2 + D^+$	$k_{26} = 1.0 \times 10^{-9} \exp(-464/T)$	4
(27)	$D + H^+ \rightarrow HD^+ + \gamma$	$k_{27} = \text{dex}[-19.38 - 1.523 \log T$ $+1.118 \times (\log T)^2$ $-0.1269(\log T)^3]$	5
(28)	$D^+ + H \rightarrow HD^+ + \gamma$	$k_{28} = \text{dex}[-19.38 - 1.523 \log T$ $+1.118(\log T)^2 - 0.1269(\log T)^3]$	5

REFERENCES.—(1) Abel et al. 1997; (2) Shapiro & Kang 1987; (3) Palla et al. 1983; (4) Galli & Palla 1998; (5) Stancil et al. 1998.

REFERENCES

Abel, T., Anninos, P., Zhang, Y., & Norman, M. L. 1997, NewA, 2, 181
Abel, T., Bryan, G. L., & Norman, M. L. 2000, ApJ, 540, 39
Beers, T., Preston, G., & Shectman, S. 1992, AJ, 103, 1987
Bromm, V., Coppi, P. S., & Larson, R. B. 1999, ApJ, 527, L5
———. 2002, ApJ, 564, 23
Bromm, V., Yoshida, N., & Hernquist, L. 2003, ApJ, 596, L135
Cen, R. 1992, ApJS, 78, 341
Chevalier, R. A. 1974, ApJ, 188, 501
Christlieb, N., Green, P. J., Wisotzki, L., & Reimers, D. 2001, A&A, 366, 898
Christlieb, N., et al. 2002, Nature, 419, 904
Cox, D. P. 1972, ApJ, 178, 159
Ferrara, A. 1998, ApJ, 499, L17
Flower, D. R. 2002, MNRAS, 333, 763
Flower, D. R., Le Bourlot, J., Pineau des Forêts, G., & Roueff, E. 2000, MNRAS, 314, 753
Flower, D. R., & Pineau des Forêts, G. 2003, MNRAS, 341, 1272
Flower, D. R., & Roueff, E. 1999, MNRAS, 309, 833
Galli, D., & Palla, F. 1998, A&A, 335, 403
Goldreich, P., & Kwan, J. 1974, ApJ, 189, 441
Haiman, Z., Thous, A. A., & Loeb, A. 1996, ApJ, 464, 523
Ikeuchi, S., & Ostriker, J. P. 1986, ApJ, 301, 522
Nakamura, F., & Umemura, M. 1999, ApJ, 515, 239
———. 2001, ApJ, 548, 19
———. 2002a, ApJ, 569, 549
———. 2002b, Prog. Theor. Phys. Suppl., 147, 99
Nishi, R., & Susa, H. 1999, ApJ, 523, L103
Nomoto, K., Iwamoto, K., Mazzali, P. A., & Nakamura, T. 1999, Astron. Nachr., 320, 265
Norris, J. F., Ryan, S. G., & Beers, T. C. 1999, ApJS, 123, 639
Omukai, K. 2000, ApJ, 534, 809

Omukai, K., & Nishi, R. 1998, ApJ, 508, 141
———. 1999, ApJ, 518, 64
Ostriker, J. 1964, ApJ, 140, 1056
Ostriker, J. P., & Gnedin, N. Y. 1996, ApJ, 472, L63
Ostriker, J. P., & McKee, C. F. 1988, Rev. Mod. Phys., 60, 1
Palla, F., Salpeter, E. E., & Stahler, S. W. 1983, ApJ, 271, 632
Panagia, N. 1973, AJ, 78, 929
Puy, D., Alecian, G., Le Bourlot, J., Léorat, J., & Pineau des Forêts, G. 1993, A&A, 267, 337
Sakashita, S., & Ikeuchi, S. 1996, Astronomical Hydrodynamics (Tokyo: Baifukan)
Salvaterra, R., Ferrara, A., & Schneider, R. 2004, NewA, 10, 113
Sedov, L. I. 1946, Prikl. Mat. Mekh., 10 (2), 241
Shapiro, P. R., & Kang, H. 1987, ApJ, 318, 32
Shelton, R. 1999, ApJ, 521, 217
Shull, J. M., & McKee, C. F. 1979, ApJ, 227, 131
Shull, J. M., & Silk, J. 1979, ApJ, 234, 427
Slavin, J. D., McKee, C. F., & Hollenbach, D. J. 2000, ApJ, 541, 218
Stancil, P. C., Lepp, S., & Dalgarno, A. 1998, ApJ, 509, 1
Taylor, G. I. 1950, Proc. R. Soc. London A, 201, 159
Tegmark, M., Silk, J., Rees, M. J., Blanchard, A., Abel, T., & Palla, F. 1997, ApJ, 474, 1
Tsujimoto, T., & Shigeyama, T. 1998, ApJ, 508, L151
Tsujimoto, T., Shigeyama, T., & Yoshii, Y. 1999, ApJ, 519, L63
Uehara, H., & Inutsuka, S. 2000, ApJ, 531, L91
Uehara, H., Susa, H., Nishi, R., Yamada, M., & Nakamura, T. 1996, ApJ, 473, L95
White, S. D. M., Efstathiou, G., & Frenk, C. S. 1993, MNRAS, 262, 1023
Yoneyama, T. 1972, PASJ, 24, 87
Yoshii, Y., & Sabano, Y. 1980, PASJ, 32, 229